CHALMERS
UNIVERSITY OF TECHNOLOGY

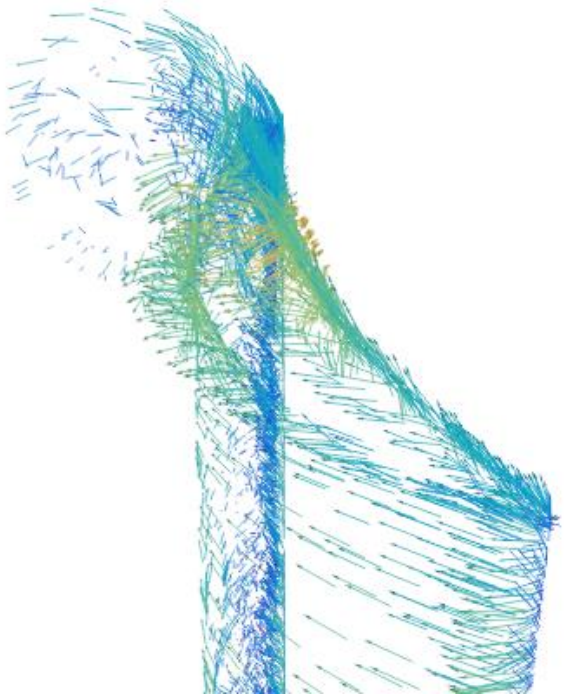

Sailing performance analysis using CFD simulations

A study on crescent shaped wing profiles

Master's thesis in Naval Architecture and Ocean Engineering

MELISA NIKMANESH

DEPARTMENT OF MECHANICS AND MARITIME SCIENCE

CHALMERS UNIVERSITY OF TECHNOLOGY
Gothenburg, Sweden 2021
www.chalmers.se

MASTER'S THESIS IN NAVAL ARCHITECTURE AND OCEAN ENGINEERING

Sailing performance analysis using CFD simulations

A study on crescent shaped wing profiles

MELISA NIKMANESH

Department of Mechanics and Maritime Sciences
Division of Marine Technology
CHALMERS UNIVERSITY OF TECHNOLOGY
Göteborg, Sweden 2021

Sailing performance analysis using CFD simulations
A study on crescent shaped wing profiles
MELISA NIKMANESH

Master's Thesis 2021:79
Department of Mechanics and Maritime Sciences
Division of Marine Technology
Chalmers University of Technology
SE-412 96 Göteborg
Sweden
Telephone: + 46 (0)31-772 1000

Cover:
Figure of 3D simulation of the initial crescent shaped wing profile which shows the velocity vectors along the tip vortex.

Department of Mechanics and Maritime Sciences
Göteborg, Sweden 2021-07-10

Sailing performance analysis using CFD simulations
A study on crescent shaped wing profiles
Master's thesis in Master's program Naval Architecture and Ocean Engineering
MELISA NIKMANESH
Department of Mechanics and Maritime Sciences
Division of Marine Technology
Chalmers University of Technology

Abstract

The global trading market is highly dependent on the shipping that takes place today. Approximately 90% of the trades is carried out on the seas, meaning that the shipping industry have a significant impact on the environment as the current internal combustion engines causes great amount of environmental pollution. A solution to this has been to study different types of renewable propulsion types in which sails are one among others. The purpose of this study is to take an initial look at a crescent shaped sail profile and how this profile relates to the reference symmetric, NACA 0015-profile.

The work of this report includes the sailing performance analysis of different parametrical changes of a crescent shaped wing profile using computational fluid dynamics, in which lift and drag coefficients are the main parameters that have been observed for 2D cases. As the validation of the software Star CCM+ was obtained for a reference profile, the crescent shaped profiles were studied. For these cases one could note much greater lift coefficients as the curvature increased and thickness was reduced.

Four different crescent shapes were studied, and within these four the thinnest of them resulted in the greatest lift. Vortices occurring along the trailing edge for the cases with the best lift was observed. The occurring of vortices indicates an increase of the drag. If the mentioned increase of drag does not affect the thrust force significantly, then the crescent shaped sail profile might be the most efficient profile for generating thrust on commercial sailing vessels.

Along the studied 2D observations an initial study of a 3D case has been carried out. In this case the induced drag could be stated, where the occurring of the phenomena of tip vortex causes a new addition of drag on to the sail. As of current studies the crescent shape wing profile still generates a greater lift than the reference NACA 0015-profile even after considering the induced drag.

Key words: Sail profile, CFD, crescent shape, NACA-0015, lift coefficient, drag coefficient, 2D & 3D

Contents

Acknowledgement

For graduating the Master's program of Naval Architecture and Ocean Engineering at Chalmers University of Technology, the fulfillment of a master's thesis is required. This thesis was carried out throughout the spring of 2021 together with the company ScandiNAOS.

In order to finalize the concept of this thesis I would like to share my gratefulness to Bengt Ramne and his team at ScandiNAOS for their patience and great support throughout the whole spring of 2021. I would like to thank my examiner and professor at Chalmers, Carl-Erik Janson and Hua-Dong Yao for giving me valuable insight into refining my work and constantly guiding me along the project. I would also share my gratefulness to Adam Persson at SSPA for sharing his valuable knowledge in computational fluid dynamics.

Lastly, I would like to give a special thanks to my family for always believing in me and supporting me through this incredible journey.

Gothenburg, June 2021

Melisa Nikmanesh

1 Introduction

Going back to the early civilizations of Egypt one can study the first recorded illustrations of monuments resembling the essentials of today's commercial shipping at least as early as 4000 B.C (Anderson & Anderson, 2003). Prior to the industrial revolution there was no configuration of motorized transportation, which signified for wind and manpower to be the principal mode of naval transportation (Rodrigue, 2020). With the extension of the industrial revolution and adaption of an efficient steam engine during 1765, the American inventor John Fitch tested the first mechanically propelled ship in 1790. Not long after the work of Fitch did a mechanized maritime shipping industry thrive, stunningly increasing the global trade.

The groundbreaking invention of the internal combustion (IC) engine states for a new complex pitfall, being the greenhouse gas (GHG) emissions. As the IC engine operating on fossil fuels provide for approximately 25% of the world's power, it thereby also stands accountable for 10% of the global GHG emissions (Reitz, o.a., 2020). Since the shipping industry constitutes for 90% of the global trading, studies have been carried out to reduce the global GHG emissions by considering renewable energy sources on ships (Shukla & Ghosh, 2009). In which by this case, wind power getting reintroduced to commercial shipping. This ancient yet new way of commercial shipping still contemplates for issues regarding the uncertainty of its capacity to counter the standard of today's global trade.

To understand the complexity of using wind propelled vessels within commercial shipping this report will give an insight over traditional sailing principals adapted on commercial vessels in which good aerodynamic performance is obtained. The report will study the case of a crescent wing shape as a solution to hopefully sustain a reasonable aerodynamic performance alongside a design in which rational limitations within the wing construction and wing cost is set for it to actually become reality. The idea of the crescent shape wing profile is to ease and enable the telescopic sail operation.

1.1 Purpose

The purpose of this study aims for the initial understanding of how the crescent shaped wing sail profile relates towards different types of parametrical comparisons of its shape. With the outline of this project, one should be able to draw reasonable conclusions for further studies into an optimal sail shape of retaining good lift conditions to validate for a significant thrust force reducing the need of combustion engines. The study aims for the 2D computational fluid dynamics comparisons of the lift and drag coefficients to later be compared as a 3D case study.

1.1.1 Limitations

The scope of this project is limited to comparing four different parametrical changes for the crescent shaped wing profile due to time the restriction of the project. When setting up the simulation model the state of the surrounding environmental circumstances, being the wind speed, the wave intensity and the wave height, sorely limited to one case study. Meaning that the attained thrust will not have taken into consideration of above stated conditions. Lastly is the used software limited to Star-CCM+.

2 Principals of sailing

To understand the aerodynamic performance of a sailing vessel it is important to initially study the basics of sailing and firstly acknowledge the direction of wind. Following sections will give a brief insight within sailing and the physics of sailing in which Newton's law, vector subtraction and Archimedes' principle among others are essential parts.

2.1 Points of sailing

In Figure **2-1** the various points of sailing are presented which refers to the course of the boat in relation to the wind (Bisbee, Halloran, & Larkin, 1995). At position 1 the boat is within the "no-go" zone, at this point the vessel is not able to sail and the sail will be luffing. At position 2 the boat is said to be closed-hauled. Here the sails should be pulled in and tight and the concept of tacking is utilized to sustain its voyage. Meaning that the boat is zigzagging in angles of approximately 45° from the wind's axis. The 3rd position represents the beam reach which generally is considered to be the fastest angle to sail at. The 4th position, called the board reach the ship is sailing slightly more downwind and thereby sails needs to be let out a bit further. As the wind direction corresponds to the centreline and direction of the vessel, the sail can be manoeuvred through either side. Thus, is the manoeuvring from one side to the other called jibing. Position 6 and 7 are similar to position 4 and 3 respectively but with a port tack on the first mentioned and starboard tack on the secondly mentioned. Finally position 8 represent the close reach, in which the sails are almost close hauled.

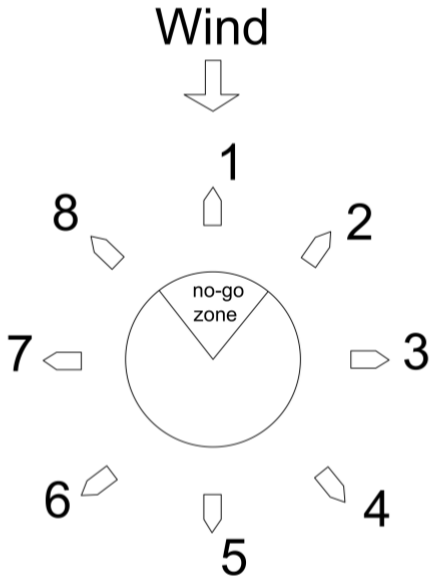

Figure 2-1 *Visualization of the points of sailing*

When considering sailing point 5 where the vessel is sailing downwind or at very high apparent-wind angels, the ambition is to increase the drag, which in this case makes the drag beneficial for the thrust force. This statement therefore means that wings utilized within sailing concepts as sails, necessarily does not need the highest lift to drag ratio similar to aviation wings.

2.2 Physics of sailing

As a fluid flows along an object, it exerts a force vector in which its components are designated as drag for the component going in the same direction as the fluid flow and lift which is the component perpendicular to the studied flow shown in Figure **2-2**.

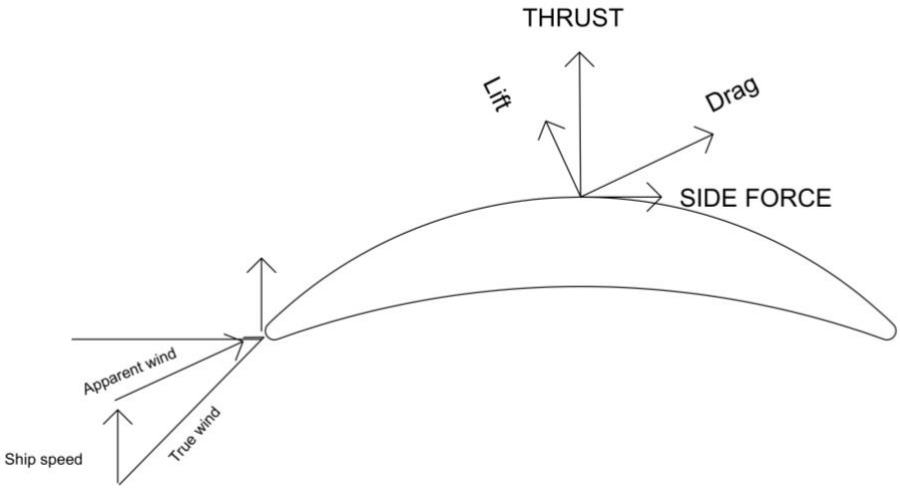

Figure 2-2 *Sail forces acting on the sail*

The lift force is generated as the fluid flows around the object and two different forces which acts on its surface occur as visualized in Figure **2-3**. One of them is due to the wall shear stresses, τ_w, and the second is the pressure, P. The first mentioned stress is tangential to the object surface, caused by frictional forces due to the fluid viscosity. The Pressure is acting perpendicular to the object surface caused by the pressure distribution along the surface.

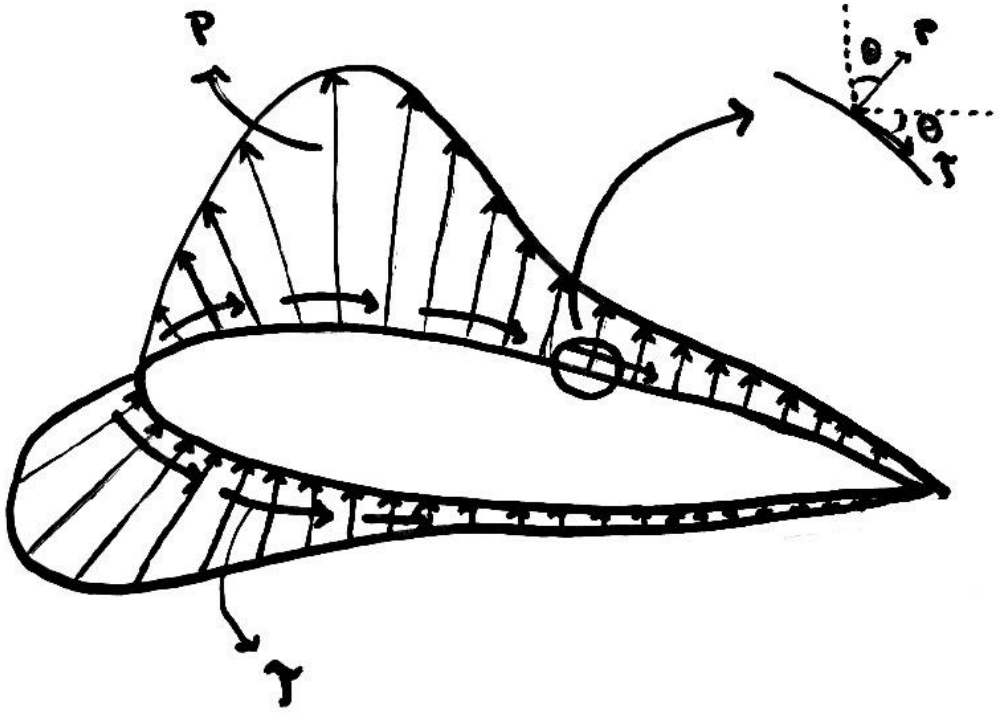

Figure 2-3 *A visualization of how the wall shear stresses and pressure acts on an airfoil*

The lift force is seemingly a resultant of the shear stress and the pressure. If the stress resultant is integrated in the lift direction over the object surface following equation 2.1 is obtained.

$$F_L = \int_A (-P \sin(\theta) - \tau_w \cos(\theta))\, dA \qquad 2.1$$

For streamline bodies such as symmetrical NACA profiles the wall shear stresses will mostly act in the same direction as the flow of the fluid and for this reason mostly contribute to the drag force. Meaning that in most cases when the lift force is studied the wall shear stresses can be neglected. Which implies that when generating lifting force pressure distribution is observed. Usually, higher pressure is established along the bottom of an airfoil and lower pressure along its top, where the suction pressure along the top is what responds to the most lifting action.

Even though it is known for the lift to be caused by differences in pressure distribution, there are not yet any clear solution on how the pressure distribution occurs. Scientists mainly argue between two concepts in which Bernoulli's principle is one of them and Newtons third law the other one.

When explaining the lifting force with Bernoulli's principle one has to initially study the stagnation point close to the leading edge. A stagnation point implies that the fluid velocity at this point is 0 *m/s*. Outside the thin boundary layer which surrounds the airfoil, the velocity of the fluid flow increases. Through the law of energy conservation, the rise of velocity leads to a reduction of pressure which causes the suction pressure to occur at the top of the airfoil. To explain the reasoning behind the velocity change one can apply the concept of mass conservation. Meaning that the streamlines above the stagnation point will be pinched together causing a geometrical change on the flow. Another point in which velocity changes is due to circulation which will be explained a bit further.

To explain the lift force caused by Newtons third law one has to recall that for every occurring action there is an equal and opposite reaction, which means for the large volume of air that is being displaced by the airfoil there should be an opposite reaction. When considering the lift force to be a result of Newtons third law one takes in account for the upwash and the downwash. Meaning that the fluid initially flows upwards along the airfoil and later is objected to a downwash. Once again one can apply the concept of circulation to explain the occurrence of the upwash and downwash.

Circulation is a key concept of describing lift, both when considering Bernoulli's principle and Newtons third law. To describe circulation, assume a curve C that fully enclosures the airfoil. The line integral of the fluid velocity around the curve shown in equation 2.2 can be said to initiate the circulation.

$$\Gamma = \oint_C V\, ds \qquad 2.2$$

Without circulation the theoretical rare stagnation point would be located slightly above the trailing edge when studying a potential flow as shown in Figure **2-4**. This occurrence

of the stagnation point would mean a rapidly sharp upward turn for the fluid flow which when studying air flow is impossible to achieve. A potential flow relates for a flow with negligible friction, as when observing a viscous flow friction of the fluid is added and is the most notable for around the boundary layer of a profile. Except for the effect of the viscosity, it can also be stated for a vortex is shed downstream in a counterclockwise direction. As the circulation in the vortex increases the stagnation point will be shifted towards the trailing edge until the Kutta condition is satisfied. The Kutta condition states that a circulation with sufficient strength to keep the stagnation point at the trailing edge is present for sharp edged bodies traveling along a flow of fluid (Kuethe & Chow, 1998).

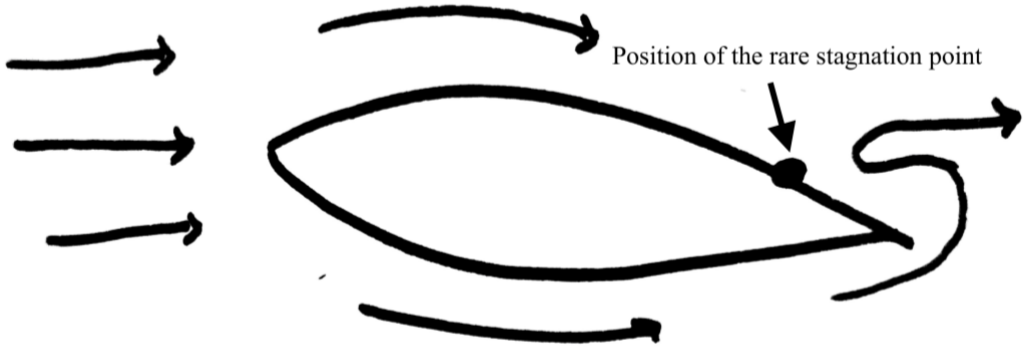

Figure 2-4 *The theoretical stagnation point if there is no circulation*

Combining the Kutta condition with Kelvin's circulation theorem, which states that the total circulation around the curve C must remain constant, results in a counteracted vortex occurrence (Eldredge, 2019). Meaning that the starting vortex gets bounced by an equal circulation in the opposite direction, induced as the circulation around the airfoil in clockwise direction matching the starting vortex. The starting vortex will eventually dissipate along the runway along due to viscosity, but the clockwise vortex will remain around the airfoil becoming the bound vortex.

The Kutta-Zhukowsky theorem sustains a method calculating the lift based on circulation which can be seen in equation 2.3.

$$L = \rho V \Gamma \tag{2.3}$$

Thus, does the theorem assume incompressible flow and also does not capture flow separation.

Similar to the lift force is the drag force induced as the resultant of the wall shear stresses and pressure in the direction of the flow, which means that by integrating them along the drag direction the drag force can be obtained through equation 2.4.

$$F_D = \int_A (-P\cos(\theta) + \tau_w \sin(\theta))\, dA \tag{2.4}$$

The drag caused by the shear stresses is denoted as the friction drag, and the drag caused by the pressure is denoted as pressure drag. The latter mentioned is more dominant in

along blunt shapes since the pressure drag increases as flow separation increases, which is when the fluid boundary layer detaches from the object of study, creating a wake of recirculating flow. To reduce drag forces, one thereby needs to reduce the amount of flow separation. Usually for bodies travelling through fluids, streamlined shapes are preferred to minimize the amount of flow separation.

When very little to no flow separation is observed, most of the total drag will be induced through the friction drag. As fluid viscosity and surface area of a body increases so does the friction drag. Opposite to pressure drag friction drag is reduced within laminar flows. This is due to the velocity profiles of the laminar and turbulent velocity profiles, see Figure **2-5**. For turbulent boundary layers the velocity gradient along the wall is steeper than the velocity gradient for laminar boundary layers, which is the reasoning for why turbulent flow induces larger frictional stresses.

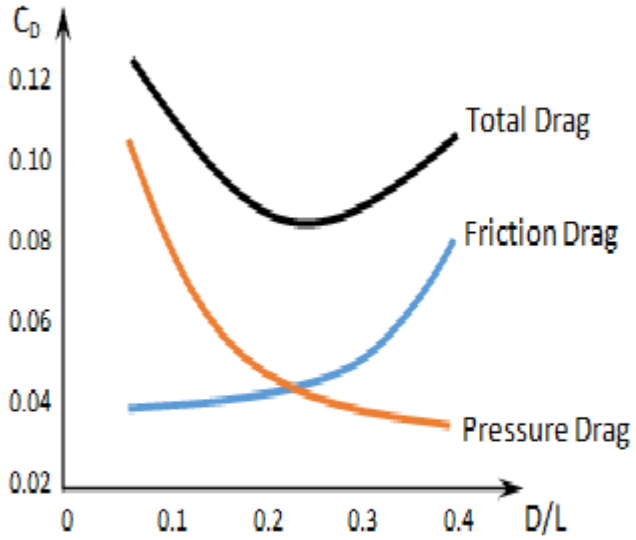

Figure 2-5 *An example of how pressure and friction drag oppositely correlates along the airfoil. D represents the thickness of an airfoil profile and L the chordlength. From: Trade-off relationship between pressure drag and friction drag [Figure], by Eshaan, (2013), Wikimedia Commons (https://commons.wikimedia.org/wiki/File:Pressure_Drag_and_Friction_Drag.png). CC BY-SA 3.0.*

To obtain the optimal airfoil shape therefore does not necessarily mean that the most streamlined body is the ideal shape since it needs to take in to account for both pressure and friction drag. To obtain detailed information about the distributions of the stresses in equation 2.4 is for many cases excessively difficult and thereby also hard to assess reasonable results. For this reason, equation 2.5 is utilized to set a representative value for the drag force.

$$F_D = \frac{1}{2} C_D \rho V^2 A \qquad 2.5$$

Where C_D represents the drag coefficient and concludes uncertain values that initially are hard to estimate. ρ represents the fluid density, V constitutes for the free-stream velocity and A stands for the reference area, which for most streamline bodies can be stated as the surface area.

Other important forms of drag to take in account for are denoted as induced drag and interference drag. The first mentioned is cased due to the finite length of a body traveling through a fluid and the pressure differences above and below the wing causes a spill-over effect occurring from the high pressure underneath the body towards the low pressure on the top of the body. This will initiate wing tip vortices that further on creates an impact on the pressure distribution around the body and create another drag component, induced drag.

Interference drag occurs anywhere where airflow from different components gets mixed together, usually existent along the base of a wing. To reduce this type of drag one can avoid interfering different components along a body with sharp edges.

2.2.1 Flow separation

As a flow of fluid travels upwards along an object initially an acceleration occurs which decreases the pressure along the surface creating a favorable pressure gradient, $\frac{\partial p}{\partial x} < 0$. When reaching a certain point, the flow will eventually decelerate which causes an increase of pressure creating the adverse pressure gradient, $\frac{\partial p}{\partial x} > 0$ that significantly affects the flow close to the wall. With the presence of a pressure increase large enough the flow will initially reverse its direction. Due to the already oncoming fluid flow, the reversed fluid will not be able to travel backwards which will cause a detachment from the surface leading to flow separation illustrated in Figure **2-6**.

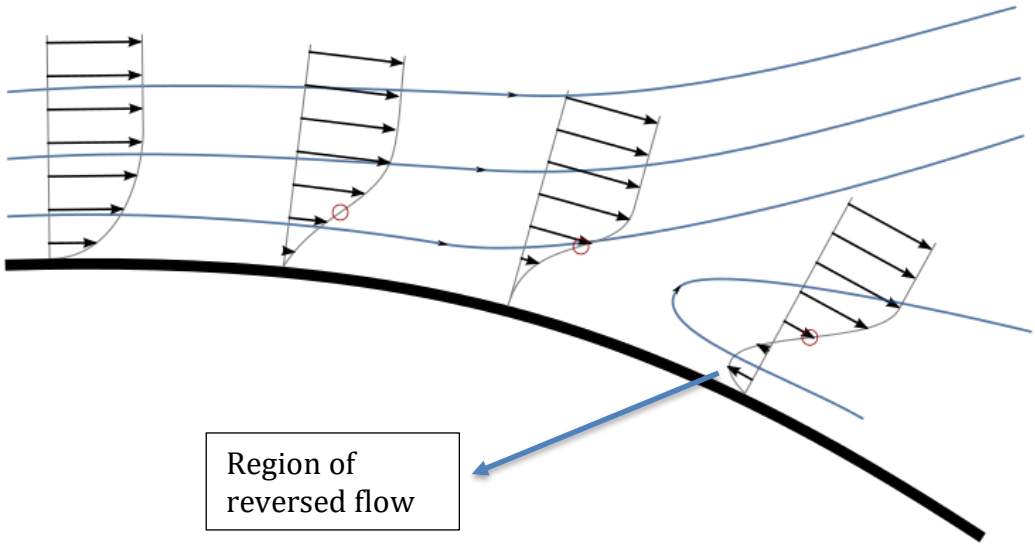

Figure 2-6 *Illustration of the occurrence flow separation. Boundary layer separation [Figure], by Olivier Cleynen, (2013), Wikimedia Commons (https://commons.wikimedia.org/wiki/File:Boundary_layer_separation.svg). CC BY 3.0.*

Flow separation causes vortex shedding which might generate unwanted vibrations and instability. To delay the occurrence of flow separation turbulent flow is a preferred form of flow. The reasoning behind this is that turbulent flow introduces a lot of mixing between the different layers of flow and this momentum transfer initiates for the flow to sustain a larger adverse pressure gradient to minimize the amount of flow separation.

2.3 Flapped wing sails

Sails being applied on commercial ships have not been a groundbreaking innovation as this concept was adapted centuries ago (Anderson & Anderson, 2003). Although the concept was disregarded along the era of industrialization and invention of the internal combustion engine (Rodrigue, 2020), the idea of reinvesting in renewable energy sources grew back throughout the first oil crisis in the 1970s (Li, Nihei, Nakashima, & Ikeda, 2015). The idea also became reality, and the modernized sails of this era was studied to reduce around 10% of the fuel consumption (Matsumoto, Inoue, & Sudo, 1983).

Since the first oil crisis and the necessity of other driving mechanisms, different sail optimizations have been studied and suggested for usage to decrease the oil consumption even further, suggestions such as cascade hard sails (Li, Nihei, Nakashima, & Ikeda, 2015) and flapped wing sails (Ahmed, Amin, Islam, & Ahmed, 2013). In both cases better lift has been sustained. For a studied experimental case in which a rigid wing sail adapted on a 7.2-meter catamaran, a matter of increased performance could be demonstrated (Elkaim & Parkinson, 2001).

Other concepts of flapped wing have also been researched upon, such as the double-flap wing profile (Li, Zhang, Li, Dai, & Li, 2019) which can be observed for in Figure **2-7**. Here can the lift and drag forces, FL and FD together with the thrust force, T and side force N be observed, given that the drag force is in the direction of the apparent wind and the lift force perpendicular to this direction.

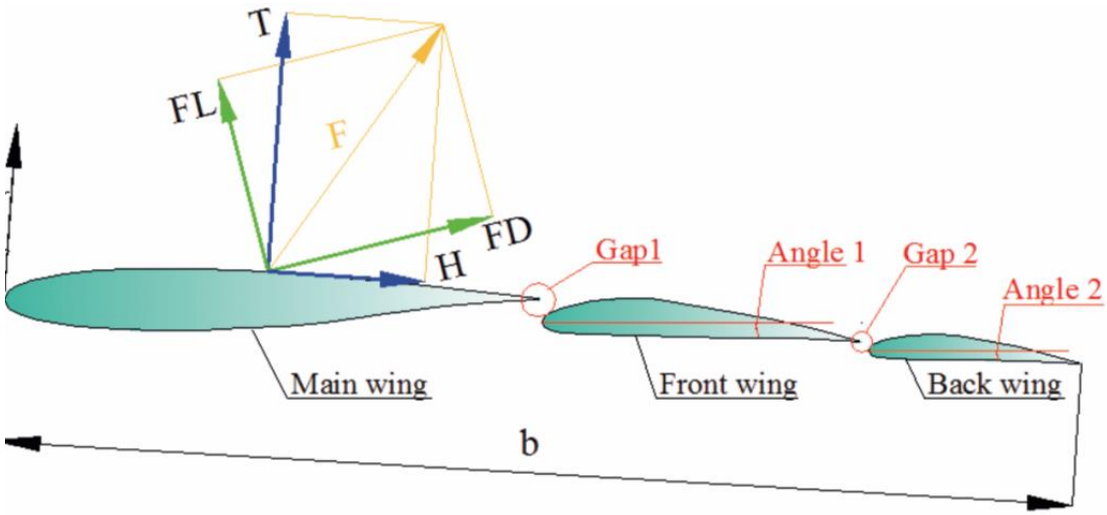

Figure 2-7 *Visualization of the double-flap wing profile. [Figure], by Dongqin Li, Yili Zhang, Peng Li, Jingjing Dai, Guohuan Li, (2019), Polish Maritime Research 4, 26(104), "Aerodynamic performance of a new double-flap wing sail".*

When comparing this type of sail wing with traditional sails such as both a NACA 0012 profile and an arc sail and a variable camber sail, one notices a remarkable performance accomplishment. It is described how the addition of a wing enlarges the area of the sail and changes the camber to retain an increase of the lift force (Li, Zhang, Li, Dai, & Li, 2019). In following Table **2-1** the lift and drag coefficients for a prototype double-flap wing from CFD simulations are presented.

Table 2-1 *Lift and drag coefficients for a double-flap wing*

Wind angle [°]	Lift coefficient, C_L	Drag coefficient, C_D
0	-0.30	0
5	0.80	0.04
10	0.55	0.07
15	0.57	0.13
20	0.70	0.23
25	1.27	0.40
30	1.60	0.60
35	1.68	0.80
40	1.33	1.00
50	0.88	1.38
60	0.71	1.64
70	0.44	1.85
80	0.18	2.24
90	-0.12	2.32

Even tough flaps generate a greater lift rather than sorely using a symmetric NACA-profile, a telescopic configuration will be hard to attain due to its manufacturing complexity. This is what makes the crescent shaped sail more interesting to study as it will create a geometrically more suitable solution for telescopic concepts.

3 Computational Fluid Dynamics

Fluid dynamics is a further branching of fluid mechanics in which flows of fluids are described (Mises & Friedrichs, 1971). The system of fluid dynamics concludes in the use of empirical and semi-empirical laws from the derivation of flow measurements to sustain solutions for a studied fluid. Following chapter will conclude in the fundamental results of classical fluid dynamics within computational fluid dynamics to the required extent for understanding the content of this report.

3.1 Fluid dynamics

The equations that govern fluid motion can be provided a numerical approximation through computational fluid dynamics (Zawawi, o.a., 2018) in which firstly the mathematical equations describing the fluid flow is written. For cases of turbulent flow, the physical circumstances increase in complexity and nearly impossible to solve without computational models for turbulent flows (Blazek, 2001).

A general definition of turbulence can be considered as Hinze (1975) once defined:

> *"Turbulent fluid motion in an irregular condition of flow in which the various quantities show a random variation with time and space coordinates, so that statistically distinct average values can be discerned"*

Reynolds-averaged turbulence is a widely used concept for understanding turbulence modelling within computational fluid dynamics which is known as RANS, Reynolds-averaged Navier–Stokes equations. It is a time averaging decomposition of the Navier-Stokes equation where each solution variable ϕ in the instantaneous Navier-Stokes equation decomposes to its mean value $\bar{\phi}$ and its fluctuating value ϕ' giving following statement:

$$\phi = \bar{\phi} + \phi' \qquad 3.1$$

The Navier-Stokes equation is composed by the three governing equations in which mass, momentum and energy conservation are the fundamental consideration (Kwang-Yong, Abdus, Ernesto, & Benini, 2019). The mass conservation equation indicates on how the rate of change of mass inside the observed volume equivalents to the sum of all fluid masses flowing inside and outside the observed volume per unit time per unit volume.

Through Newton's second law, which establishes that the force applied on a body to be directly proportional to the rate of change of momentum (Zimba, 2009), the momentum-conservation equation is composed (Kwang-Yong, Abdus, Ernesto, & Benini, 2019).

3.2 Spalart-Allamaras turbulence model

Through the era of 1950's four categories of turbulence were established. First being the algebraic (zero-equation) models then the one-equation and two-equation models and lastly the stress-transport models.

The Spalart-Allamaras turbulence model is a one-equation, RANS-based model that solves the transport equation for the modified diffusivity $\tilde{\nu}$ shown as equation 3.3, the kinematic eddy viscosity is stated as equation 3.2 (Spalart & Allmaras, 1992).

$$\nu_T = \tilde{\nu} f_{v1} \tag{3.2}$$

$$\frac{\partial \tilde{\nu}}{\partial t} + U_j \frac{\partial \tilde{\nu}}{\partial x_j} = c_{b1}\tilde{S}\tilde{\nu} - c_{w1} f_w \left(\frac{\tilde{\nu}}{d}\right)^2 + \frac{1}{\sigma}\frac{\partial}{\partial x_k}\left[(\nu + \tilde{\nu})\frac{\partial \tilde{\nu}}{\partial x_k}\right] + \frac{c_{b2}}{\sigma}\frac{\partial \tilde{\nu}}{\partial x_k}\frac{\partial \tilde{\nu}}{\partial x_k} \tag{3.3}$$

Where the closure coefficients and auxiliary relations are related as stated below.

$$c_{b1} = 0.1355, \qquad c_{b2} = 0.622, \qquad c_{v1} = 7.1, \qquad \sigma = 2/3$$

$$c_{w1} = \frac{c_{b1}}{\kappa^2}\frac{(1+c_{b2})}{\sigma}, \qquad c_{w2} = 0.3, \qquad c_{w3} = 2, \qquad \kappa = 0.41$$

$$f_{v1} = \frac{\chi^3}{\chi^3 + c_{v1}^3}, \qquad f_{v2} = 1 - \frac{\chi}{1+\chi f_{v1}}, \qquad f_w = g\left[\frac{1+c_{w3}^6}{g^6 + c_{w3}^6}\right]^{1/6}$$

$$\chi = \frac{\tilde{\nu}}{\nu}, \qquad g = r + c_{w2}(r^6 - r), \qquad r = \frac{\tilde{\nu}}{\tilde{S}\kappa^2 d^2}$$

$$\tilde{S} = S + \frac{\tilde{\nu}}{\kappa^2 d^2} f_{v2}, \qquad S = \sqrt{2\Omega_{ij}\Omega_{ij}}$$

Here Ω_{ij} is the rotational tensor and d is the distance from the closest surface. By considering $\tilde{\nu}$ rather than the turbulent kinetic energy K, as the conveyed feature the Spalart-Allmaras model simply bypasses the need of an algebraic expression for turbulent length scale (Ghiaasiaan S, 2012). This is a one-equation model considered to be a relevant option for computationally intensive aerodynamic simulations, but rarely used for problems concerning heat or mass transfer. The model does also have its drawbacks regarding free shear flow cases (AIAA, 2019). Meaning that the model will condemn for major deficiencies when inhomogeneous flows with mean velocity gradients developed in the absence of boundaries are studied.

4 Method

The thesis aims for observing the efficiency of a crescent shaped wing profile compared to already existing NACA-0015 il symmetric profile and the efficiencies of adding extra flaps on the trailing edge.

Initially a simulation of the symmetrical profile was carried out to test the accuracy of the setup with already measured values of the profile. As the setup were considered accurate enough, batch simulation running through different angles of attack on the crescent shaped profile was carried out. Angles between 0° to 25° were studied. Results were later compared with current flapped-wing studies through polar plot comparisons for the thrust force with the observed lift and drag coefficients.

To analyze the induced drag caused by tip vortices which is an essential part for studying the drag, an initial 3D simulation was set up.

4.1 Studied profiles

Alongside the symmetrical NACA 0015-profile following four profiles shown in Figure **4-1** and Figure **4-2** were studied. These profiles indicate for changes in curvature and thickness. The profiles are named as D2R10 for the initial crescent case, D2R12 for the profile with a decreased curvature, D2R9 for the profile with increased curvature and D1R10 for the profile with reduced thickness.

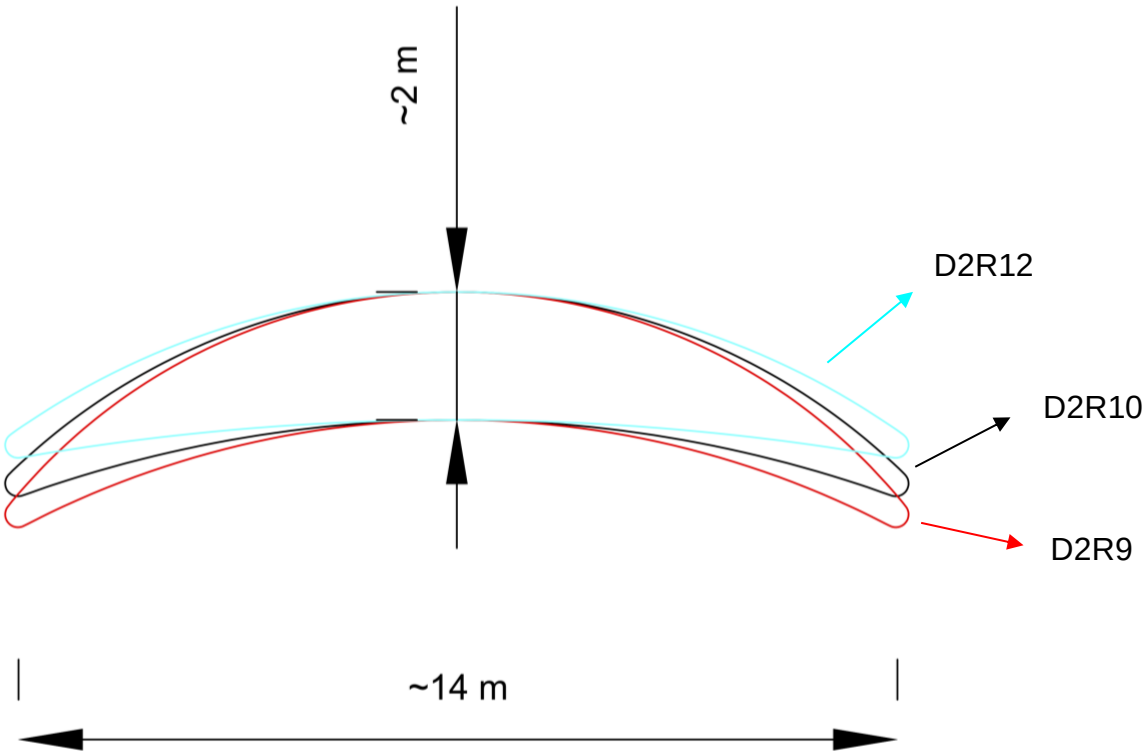

Figure 4-1 *The different curvature parametrizations of the crescent shaped wing profile where the blue line represents the decreased curvature, the black line represents the initial model and the red line the increased curvature*

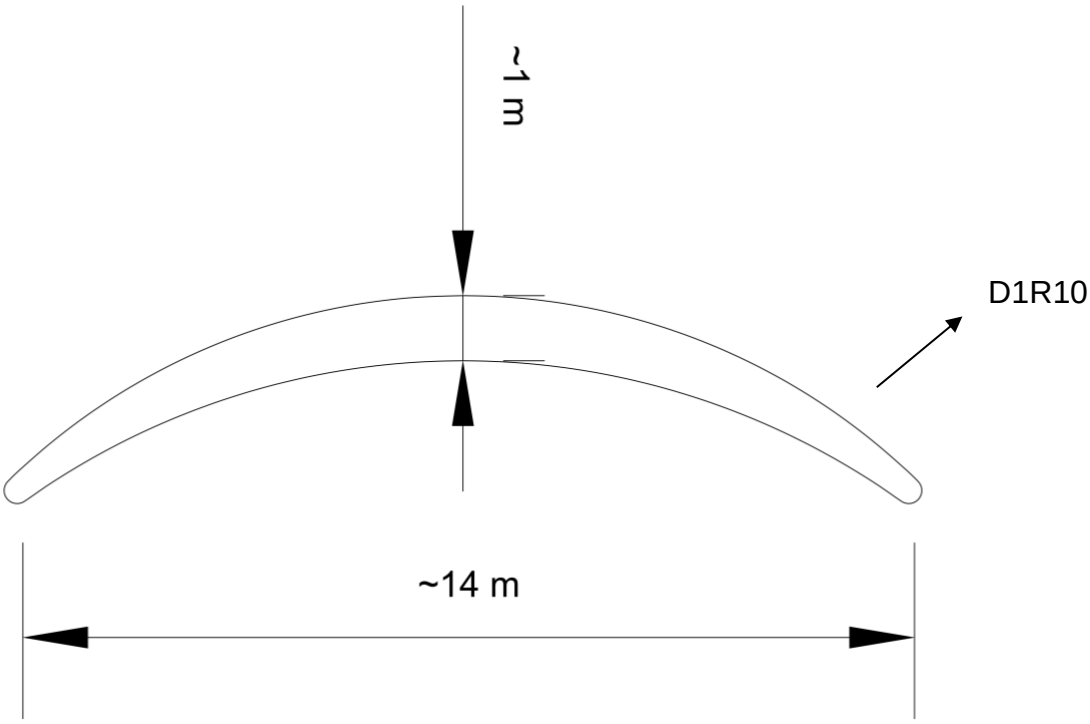

Figure 4-2 *The crescent shaped wing profile with a parametrization change of reduced thickness*

Note that the parametric difference between D1R10 and D2R10 is the thickness.

4.2 Simulation setup

The airfoil shapes were added to the software Star CCM+ accordingly to the format in which they were given. The symmetric profile was studied as the NACA-0015 il airfoil in which datasets were gathered through its website (Airfoil Tools, 2021) to obtain adequate numbers of coordinates in .csv format. The crescent shaped profile model where given from the company ScandiNAOS as an .iges file, in which coordinates could be obtained. Figure **4-3** illustrates for the general steps needed to carry out a CFD simulation for both 2D and 3D simulations.

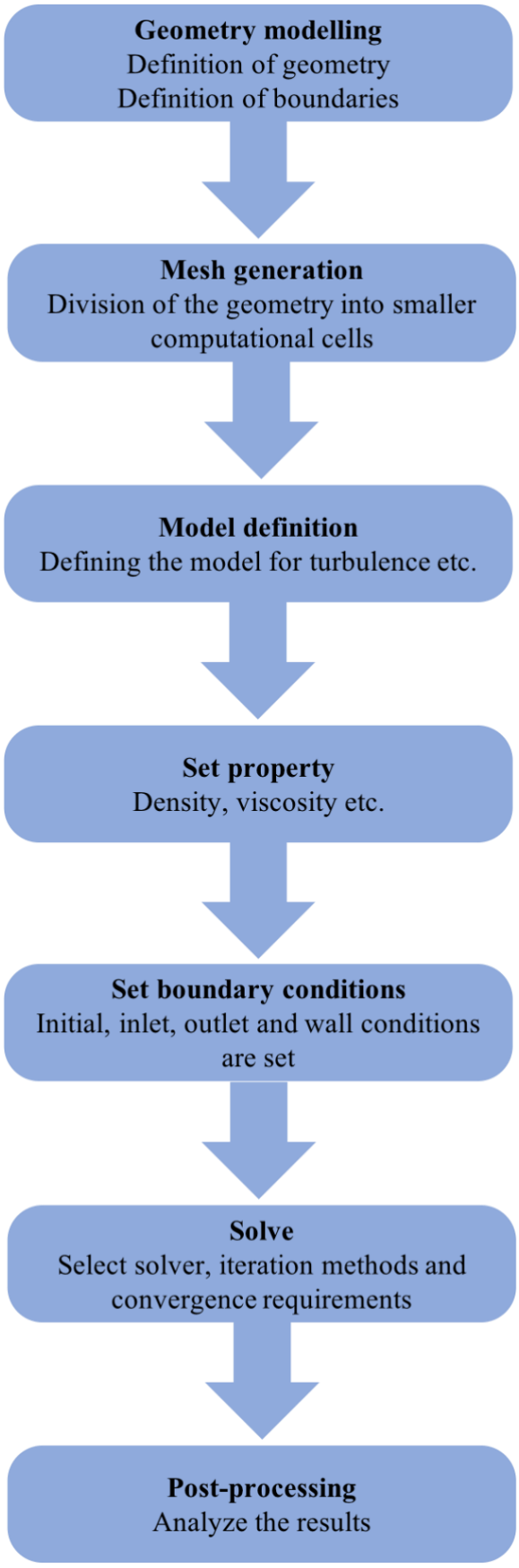

Figure 4-3 *Steps in CFD*

4.2.1 2D simulation

To obtain accurate solutions form the simulation adequate meshing had to be carried out. Similar meshing formats were used for both the symmetrical profile and the crescent shaped profile. According to the software guidelines from Siemens (n.d), recommended domain settings would be a “bullet-shaped” far field boundary in which the domain extents should be approximately 10 body lengths. It is also stated that the mesh size on current domain typically could be in the order of the body length.

Polygonal mesher is selected alongside with prism layer meshing. Default controls were set accordingly as Table **4-1** which are values designated from calculations of the turbulent boundary layer along a flat plate. Considering these values where no further mesh refinement was carried out.

Table 4-1 *Simulation settings under default controls for 2D meshing*

Automated Mesh (2D)	
Base Size	6.85 m
CAD Projection	Default
Target Surface Size	Relative to base → 1.0 %
Minimum Surface Size	Relative to base → 0.1 %
Surface Curvature	# Pts/circle → 72.0
Surface Proximity	Default
Surface Growth Rate	User specified → 1.15
Number of Prism Layers	41
Prism Layer Stretching	1.2
Prism Layer Total Thickness	Absolute → 0.18 m

Modifications had to be carried out on the mesh along the leading and trailing edges and the domain inlet and outlet. Therefore, three different custom controls were added accordingly as Table **4-2**.

Table 4-2 *Simulation settings under custom controls for 2D meshing*

Automated Mesh (2D)	
Inlet and Outlet	
Target Surface Size	Relative to base → 100 %
Minimum Surface Size	Relative to base → 100 %
Prism Layers	Disable
Leading Edge	
Target Surface Size	Relative to base → 0.1 %
Minimum Surface Size	Relative to base → 0.05 %
Trailing Edge	
Wake Refinement	Enabled
Distance	15.0
Spread Angle	20 deg
Isotropic Size	5.0 %
Growth Rate	1.3

Figure **4-4**, Figure **4-5** and Figure **4-6** represents the mesh with above mentioned settings.

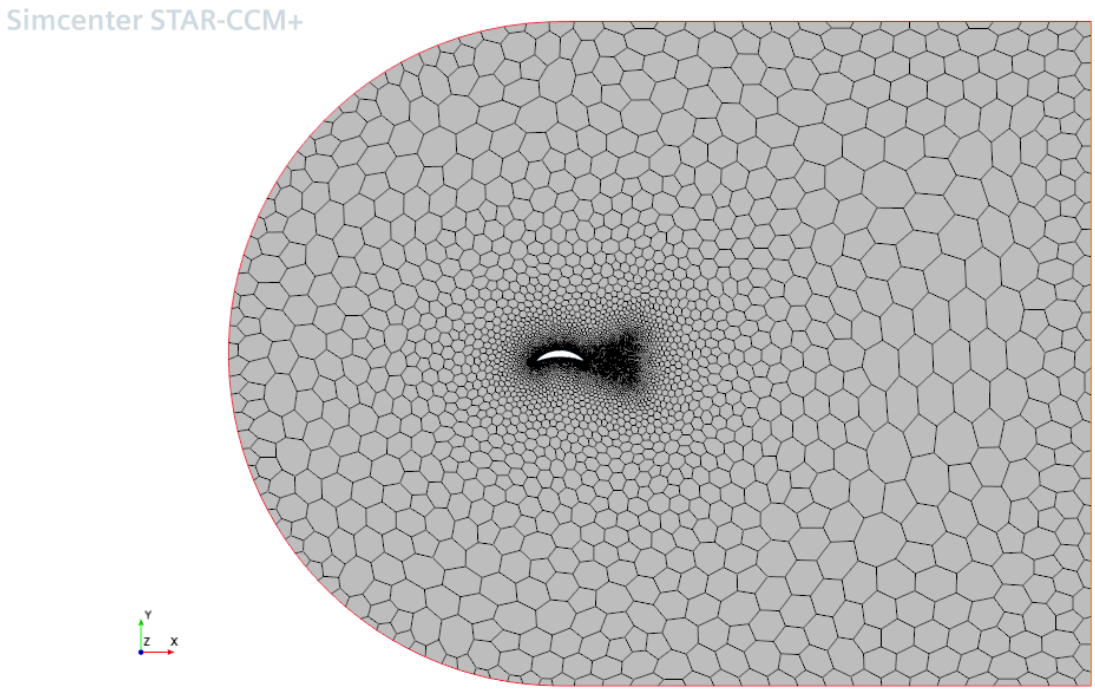

Figure 4-4 *The mesh for the crescent shaped profile*

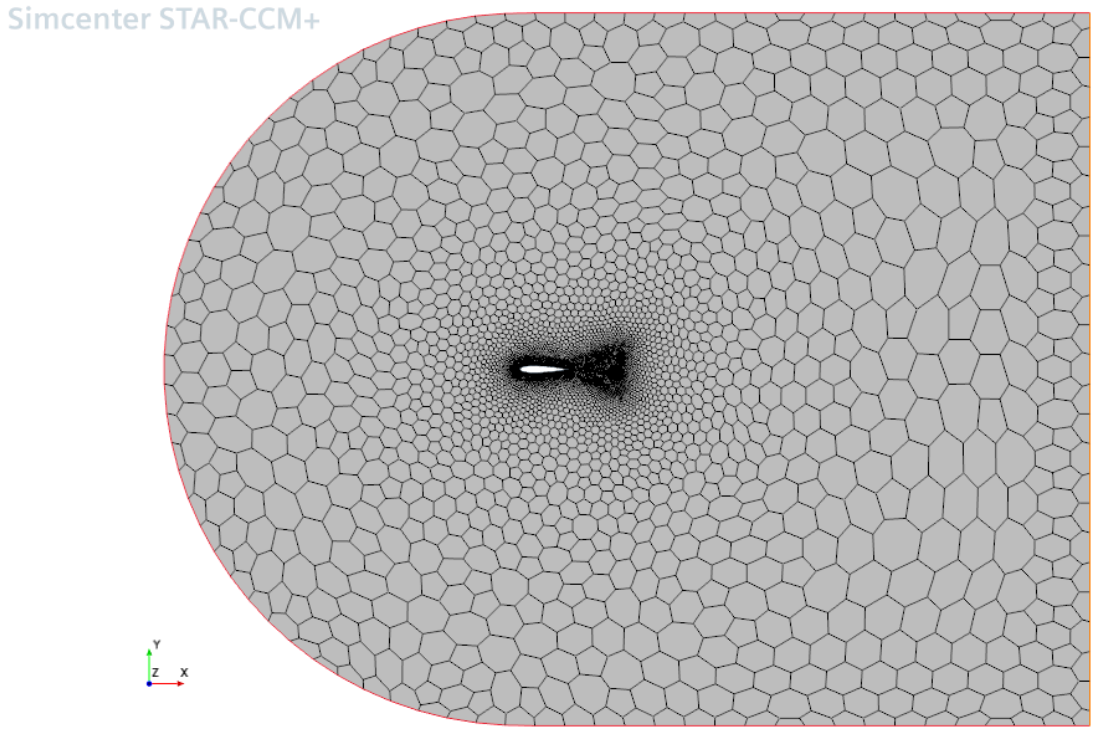

Figure 4-5 *The mesh for the NACA 0015-il profile*

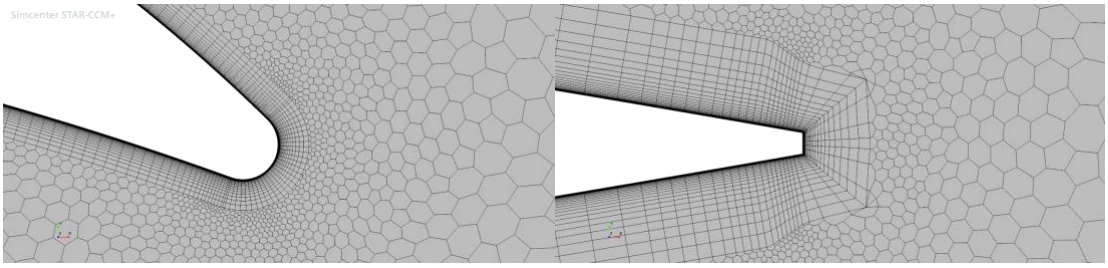

Figure 4-6 *A close up of the meshes where the crescent profile is observed on the left and the NACA-0015-il on the right-hand side*

The physics model in the software was built up with the below stated settings for a time step set at 0.001 s.

- Constant density model
- Single component as material model
- Implicit unsteady model, URANS
- Reynolds-averaged Navier-Stokes
- Segregated flow model
- Spalart-Allmaras turbulence model
- Two-dimensional model

4.2.2 3D simulation

For studying the 3D case the same turbulence model was set up as the 2D case. The domain of the simulation was set up as 5 times higher than the chord length of the airfoil as presented in Figure **4-7**.

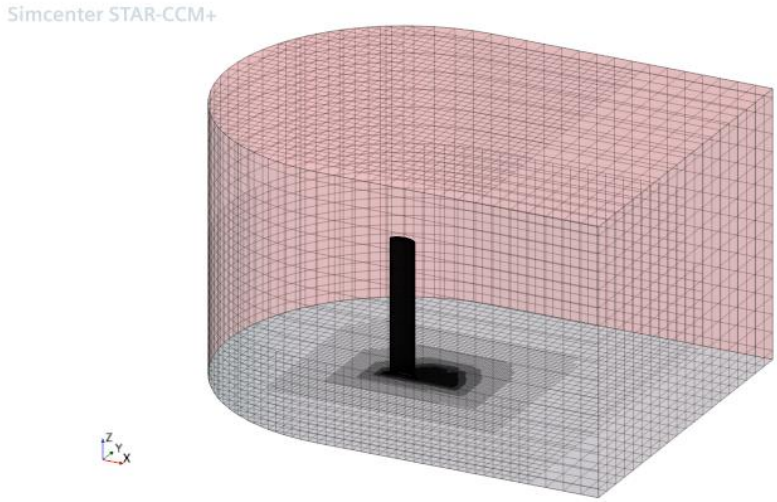

Figure 4-7 *Meshing of the 3D crescent shaped profile*

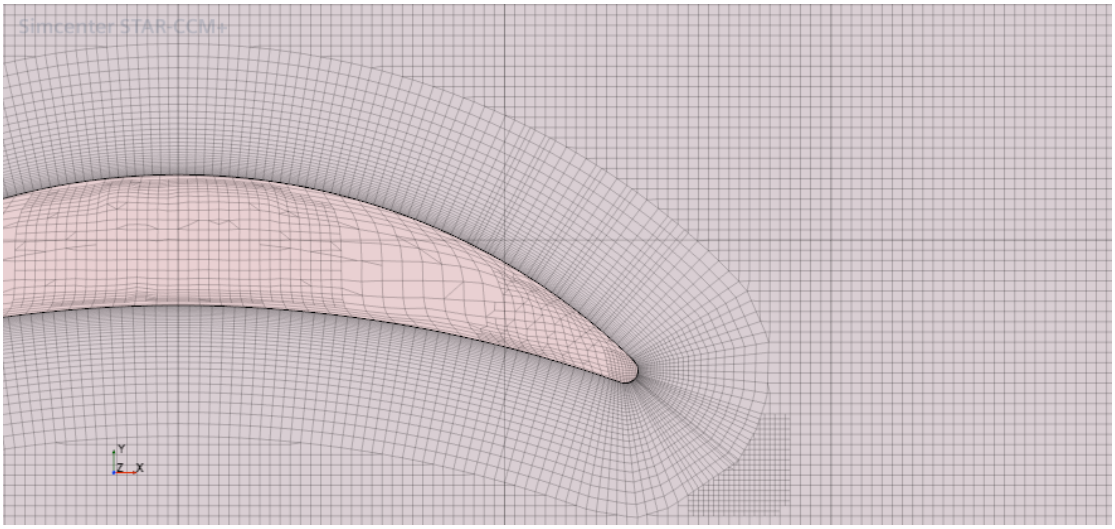

Figure 4-8 *A close up of the 3D meshing on the crescent shaped sail profile*

5 Results and discussion

In this following chapter the simulation results are presented alongside with analysis discussions. It will be discussed for the applicability of the crescent shape profile on seagoing vessels.

5.1 Lift and drag coefficients

Measured simulation data for the lift and drag coefficients gathered from Star CCM+ are presented in Table **5-1**. The presented values are stated as mean values over a certain time period in which a homogenous pattern could be studied.

Table 5-1 *Simulation results of the NACA 0015-profie with angle of attack between 0° to 25°*

Star CCM+ CFD simulations		
Reynolds number: $18.5 \cdot 10^6$		
NACA 0015		
Angle [°]	C_D	C_L
0	0.0084	0.00003
5	0.0099	0.56
10	0.014	1.1
15	0.023	1.58
20	0.048	1.8
25	0.48	1.08

When a comparison between the values in table Table **5-1** and the values of the reference data presented in Appendix A, it can be concluded that the simulation sustains reasonable accuracy. Meaning that a similar model and mesh could be carried out for the crescent shaped wing profile for a larger set of angles of attack to obtain furthermore data for the observations of this new type of wing profile. Table **5-2** displays the lift and drag coefficients of the 2D cases for the different parametrization options in which the total number of simulation results are presented in Appendix B.

Table 5-2 *Simulation results of the crescent shaped wing profile with angles of attack between 0° to 30° and alternative parametric changes*

Star CCM+ CFD simulations								
Reynolds number: $18.5 \cdot 10^6$								
Crescent wing profile								
Parametric Change	D2R9		D2R10		D2R12		D1R10	
Angle [°]	C_D	C_L	C_D	C_L	C_D	C_L	C_D	C_L
0	0.0673	0.6768	0.0483	0.9727	0.0198	0.9459	0.0502	0.7453
5	0.0893	1.7970	0.0587	1.6459	0.0291	1.3323	0.0639	1.8785
10	0.1309	2.1401	0.0899	1.9835	0.0484	1.6921	0.0966	2.2733
15	0.1881	2.3667	0.1373	2.2308	0.0850	2.0139	0.1446	2.4988
20	0.2682	2.5314	0.2123	2.3792	0.1465	2.1917	0.2203	2.6183
25	0.3873	2.5914	0.3336	2.4066	0.8451	2.3502	0.3471	2.6155
30	0.5723	2.5464	1.1896	2.3834	1.1552	2.0016	1.1451	2.4779

By reading Table **5-2** it can be confirmed for how both the lift and drag coefficient seemingly increases when comparing them to the values of Table **5-1**.

5.1.1 Lift and drag coefficient from 3D simulation

In Table **5-3** it can be followed for the results obtained from the 3D simulation of the crescent shaped wing profile D2R10.

Table 5-3 *3D simulation results of the initial (D2R10) crescent shaped wing profile with angles of attack between 0° to 25°*

Star CCM+ CFD simulations						
Reynolds number: $18.5 \cdot 10^6$						
	2D		3D		ratio	
Angle [°]	C_D	C_L	C_D	C_L	C_D	C_L
0	0.0483	0.9727	0.1698	0.8884	3.5155	0.9133
5	0.0587	1.6459	0.1879	1.2158	3.2010	0.7387
10	0.0899	1.9835	0.265	1.4358	2.9477	0.7239
15	0.1373	2.2308	0.3698	1.6925	2.6934	0.7587
20	0.2123	2.3792	0.2738	2.4155	1.2897	1.0153
25	0.3336	2.4066	0.6112	2.2659	1.8321	0.9415

From the Table **5-3** above it can be stated for how the drag coefficient seemingly has increased within the 3D simulations compared to 2D simulations. Through this statement one can thereby reckon for the induced drag which is not covered by sorely the 2D simulations. The induced drag will be discussed about further in the chapter. To notice for is also the not as drastic change of the lift coefficient. The reduction of the lift coefficient can either be a consequence of induced drag, or due to differences in meshing within the CFD software, which also can be an issue of consideration.

5.2 Velocity distribution

Following section will give an insight on how the different velocity distributions will interact depending on the shape of the sail profile. The comparisons are also here between the four different parametrizations of the crescent shaped wing and the NACA 0015-il profile.

5.2.1 2D simulation

The results of the following 2D simulations were gathered as the coefficients were observed to converge to a homogenous pattern. Figure **5-1** represents the velocity distribution for the NACA 0015-il profile for the angles 0°, 5°, 10°, 15°, 20° and 25° respectively.

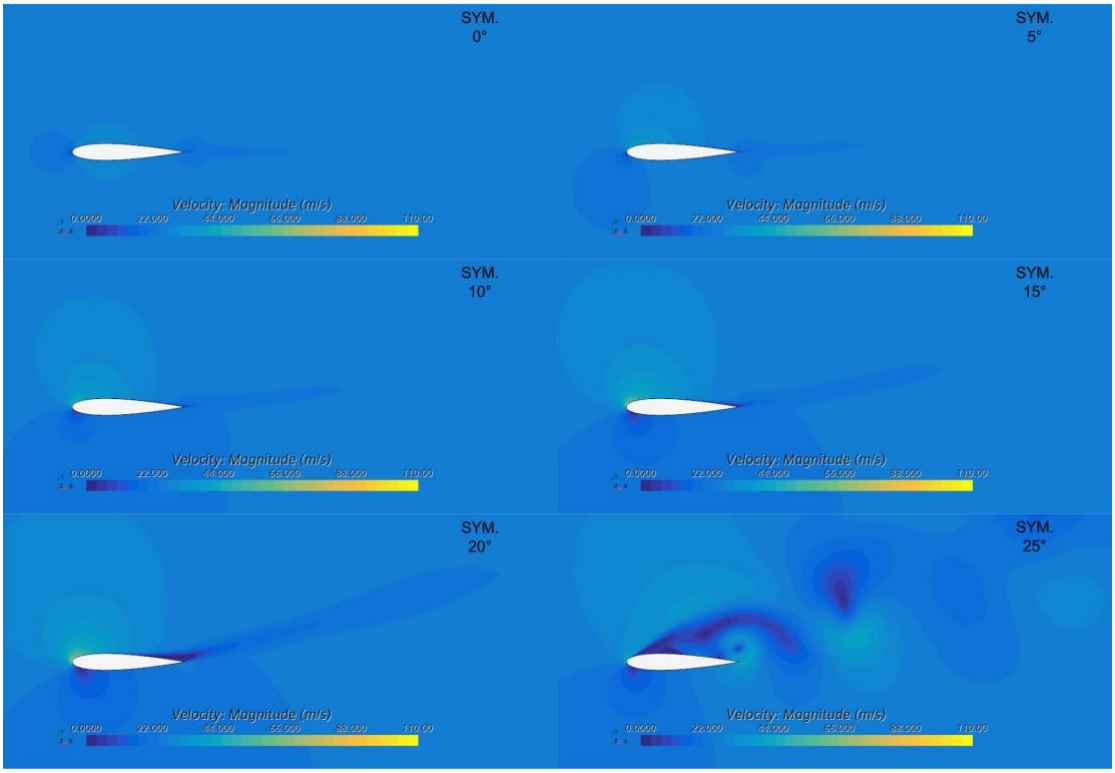

Figure 5-1 *Velocity profile for the symmetric NACA 0015-profile for angles of attack of 0° to 25° from top to bottom*

Figure **5-2** represents the velocity distribution for the initial crescent shaped wing profile for the angles 0°, 5°, 10°, 15°, 20° and 25° respectively.

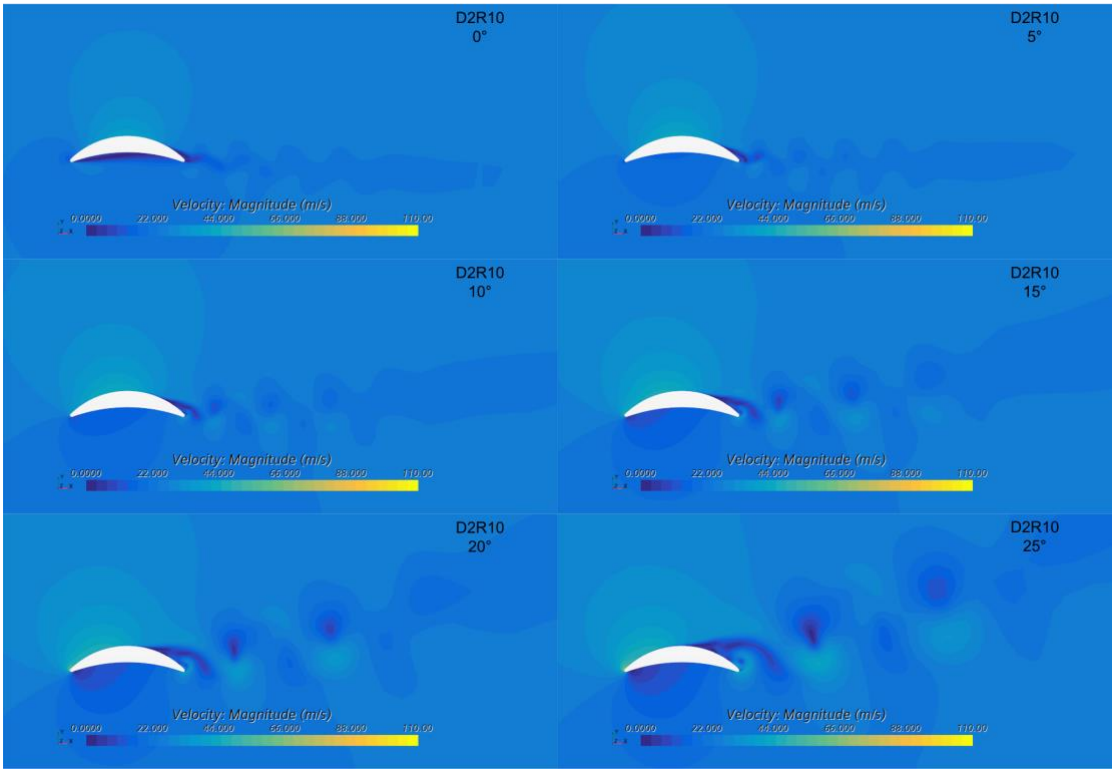

Figure 5-2 *Velocity profile for the D2R10-profile for angles of attack of 0° to 25° from top to bottom*

Figure **5-3** represents the velocity distribution for the crescent shaped wing profile with a decreased curvature for the angles 0°, 5°, 10°, 15°, 20° and 25° respectively.

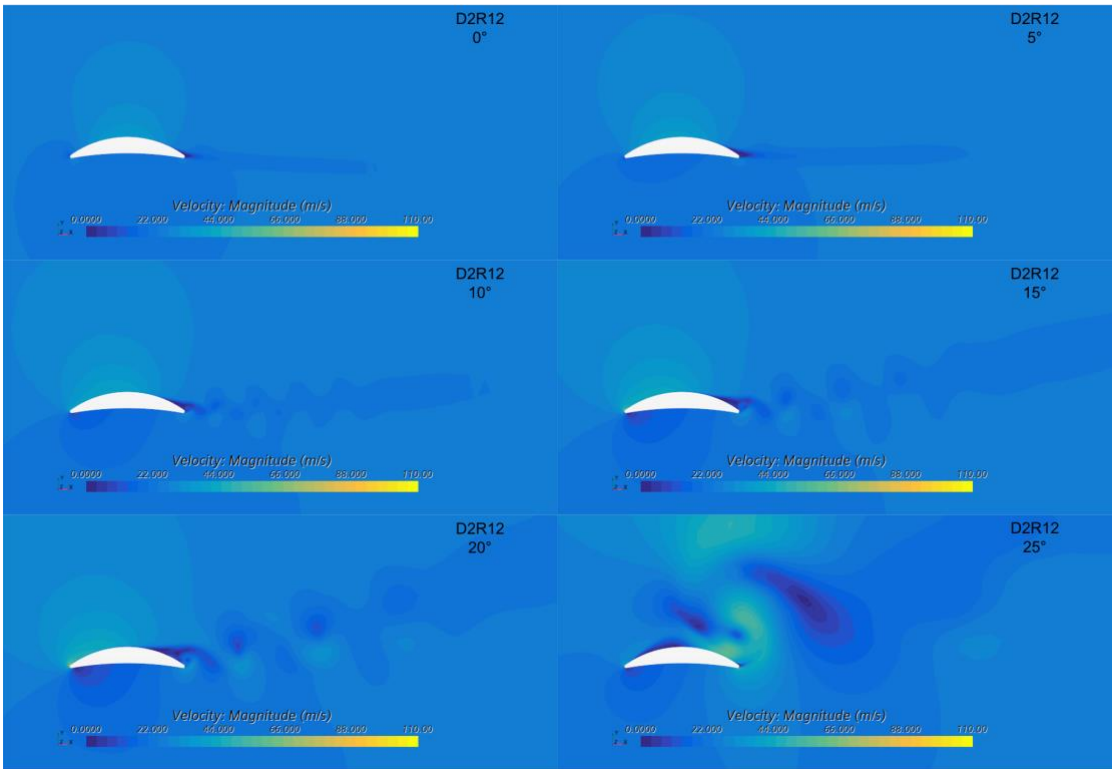

Figure 5-3 *Velocity profile for the D2R12-profile for angles of attack of 0° to 25° from top to bottom*

Figure **5-4** represents the velocity distribution for the crescent shaped wing profile with an increased curvature for the angles 0°, 5°, 10°, 15°, 20° and 25° respectively.

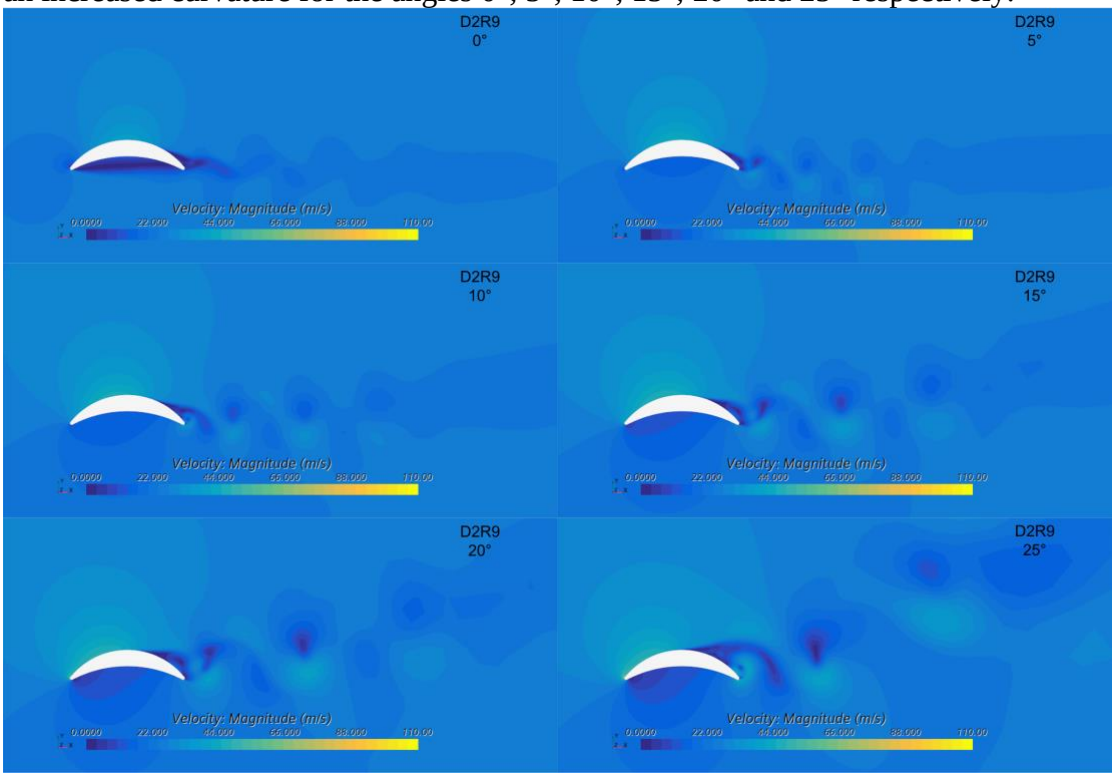

Figure 5-4 *Velocity profile for the D2R9-profile for angles of attack of 0° to 25° from top to bottom*

Figure **5-5** represents the velocity distribution for the initial crescent shaped wing profile but with a halved diameter for the angles 0°, 5°, 10°, 15°, 20° and 25° respectively.

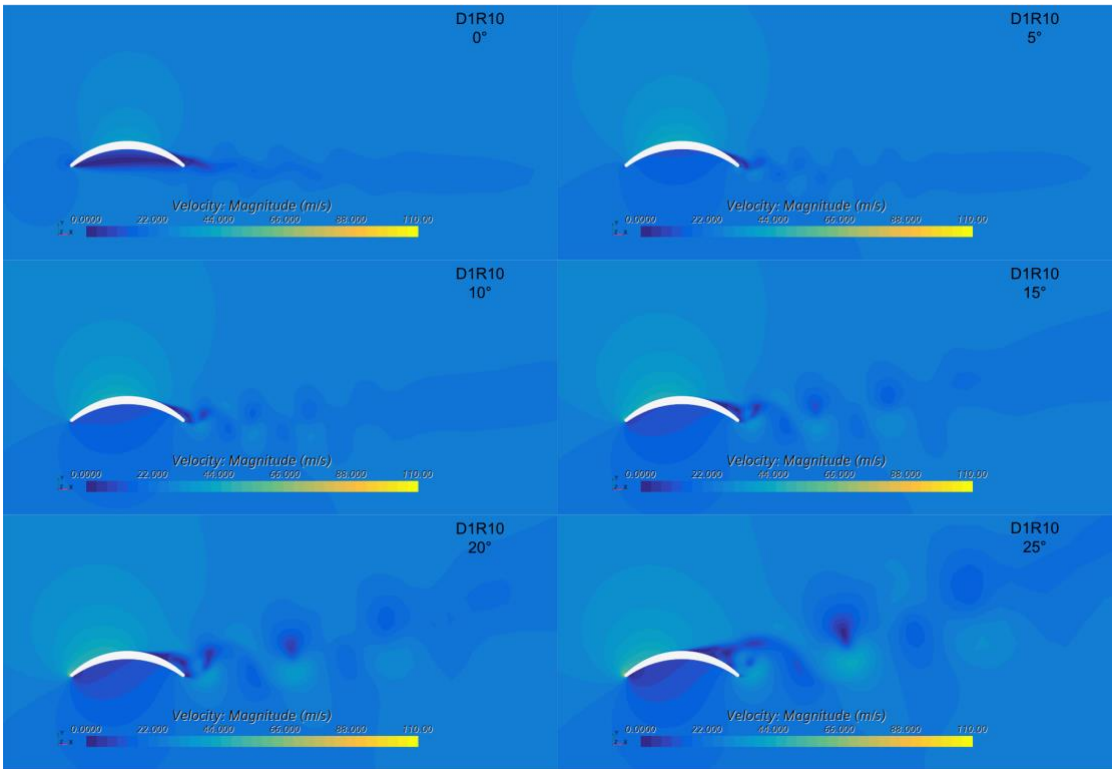

Figure 5-5 *Velocity profile for the D1R10-profile for angles of attack of 0° to 25° from top to bottom*

When studying the different cases for the crescent shaped wing profiles one can immediately notice for the increase of vortices as the curvature increases. But at the same time does these same curved profiles also induce higher velocities within the first half of the profile meaning for lower pressure and thereby resulting in a greater lift force.

5.2.2 3D simulation

Studying the velocity magnitude along the spanwise length of the crescent shaped wing sail in Figure **5-6** one can notice for differences due to effects that has not been taken into account for when sorely considering 2D simulations.

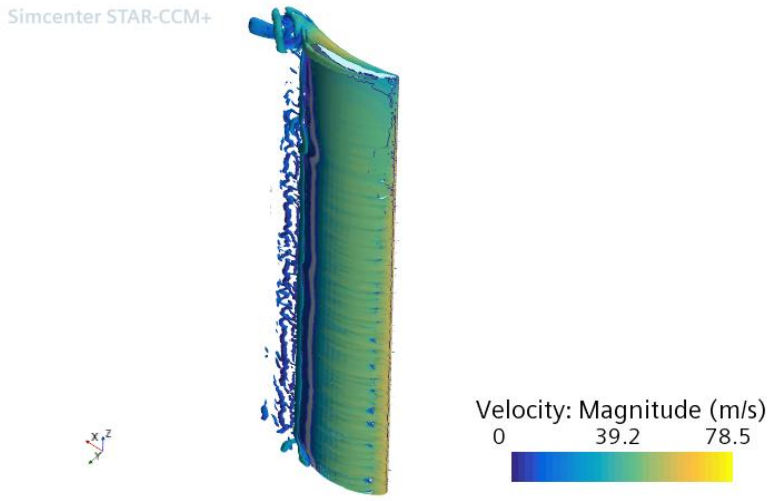

Figure 5-6 *The velocity distribution along the initial crescent shaped sail. Velocity flow in positive x-direction*

In the figure above one can notice for the change of velocity along the sail. These are due to pressure differences that occur due to the induced drag. This phenomenon will be discussed more in section 5.3.2. The Figure **5-7** gives a clearer visualization of the occurring tip vortex and shows for how it detaches from the wing causing imbalances along the sail, especially at the closer sections to the trailing edge. The "spill-over" of pressure from high pressure region to low pressure region at the suction side can be noticed for.

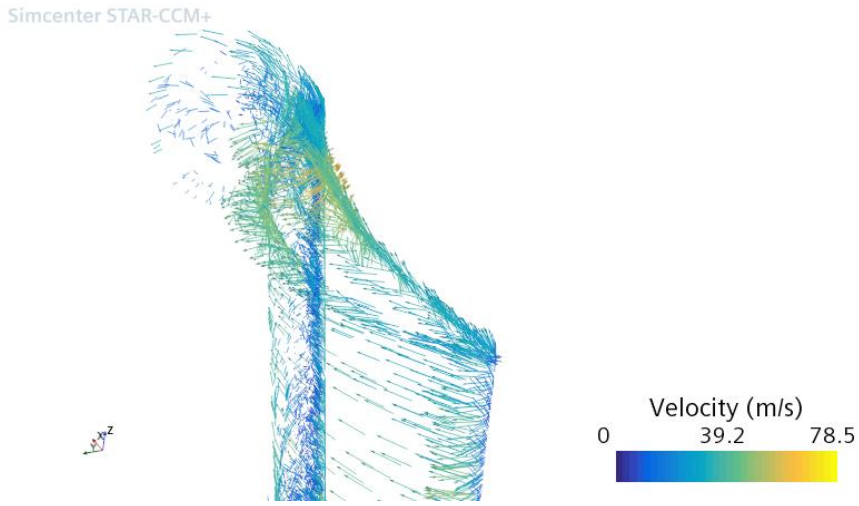

Figure 5-7 *Visualization of the flow direction of the initial crescent shaped wing profile*

5.3 Pressure profiles

Following section will give an insight on how the different pressure distributions are acting on the sail. Also here are the comparisons between the four different parametrizations of the crescent shaped wing and the NACA 0015-il profile. To consider for, is how velocity is related to pressure, meaning that for the cases when a velocity acceleration has occurred there must be a dip in pressure that will be the cause of the lift force.

5.3.1 2D simulation

Following Figure **5-8** represents the pressure profiles for the crescent shaped wing profile with the four different parametrizations in each of them for the angles 0°, 5°, 10°, 15°, 20° and 25°.

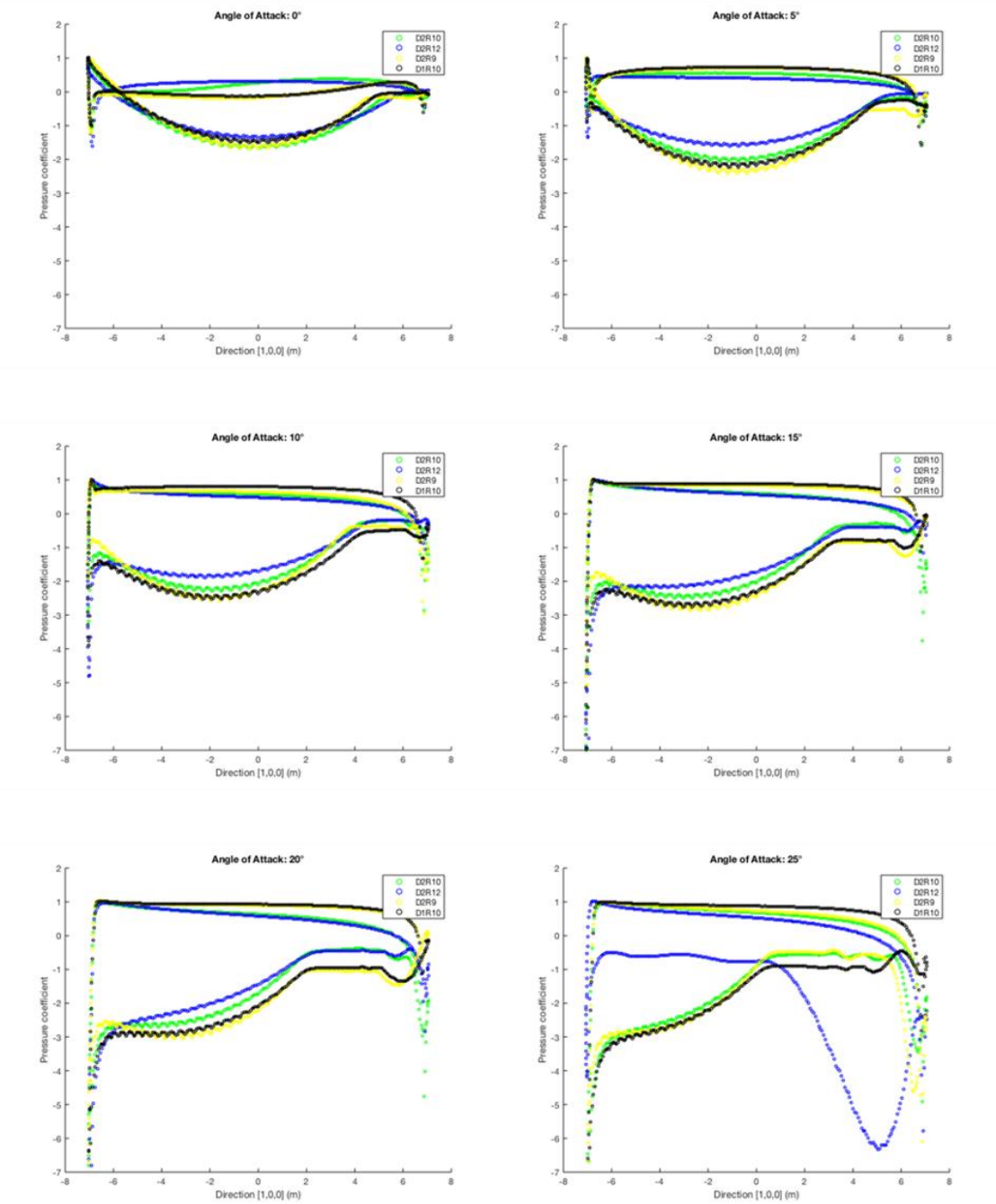

Figure 5-8 *Pressure profile for different crescent shaped wings with AoA varying from 0° to 25°*

When studying the pressure profiles for the crescent shaped wings above one can consider for the increased magnitude for lower pressure at the top of the wing when the wing sustains a thinner shape. This can specifically be noticed for within the smaller angles of attack at 5° and 10°, meaning that thinner and more rounded shapes of the wing have greater conditions of attaining better lift. Though it is the most important to observe the cases for when the angle of attack is considered at its optimum, which in

this case is seen in 20°. Studying the case when the angle of attack is set to 20 degrees one notices for a seemingly increased pressure magnitude compared to the other conditions meaning that this condition could state for an optimum where a large lifting force can be imposed.

5.3.2 3D simulation

Figure **5-9** shows for the pressure distributions along the sail profile at heights of 20, 50 and 80 % of the spanwise length.

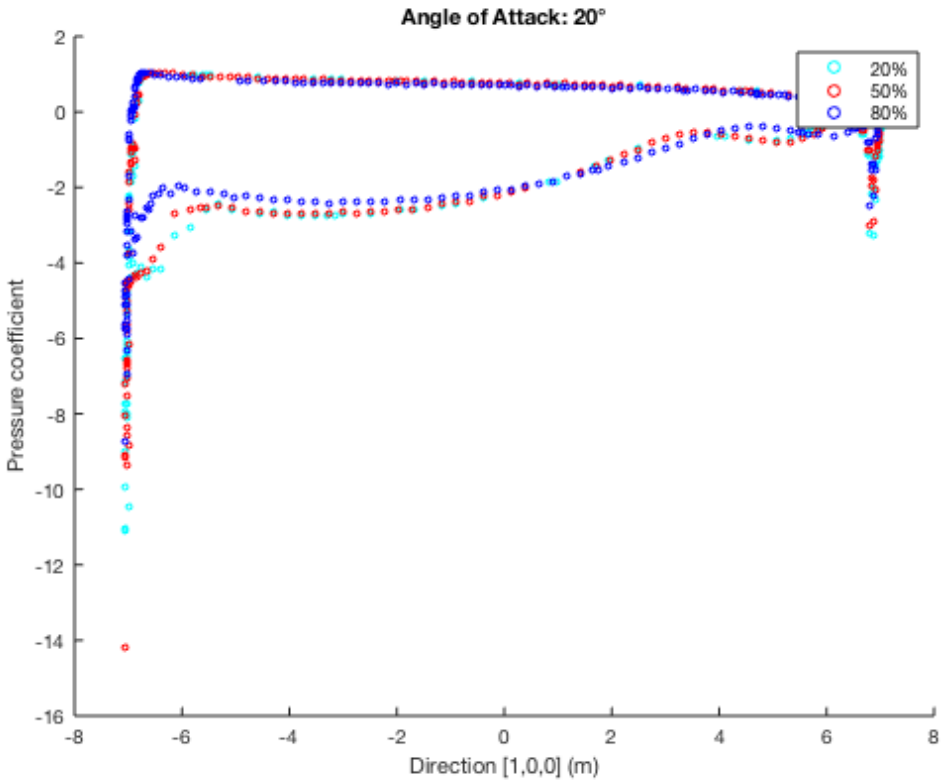

Figure 5-9 *Pressure profile for the initial crescent shaped profile for AoA 20° at different spanwise positions*

From the figure one can notice for how the pressure changes along the spanwise length of the profile. This is due to the induced drag that occurs at the tip of the wing which is caused by the phenomenon of tip vortices. The closer to the tip one is studying, the greater becomes the impact from the tip vortices, which can be observed as the 80% spanwise length reduces in its value of pressure coefficient especially at leading edge.

5.4 Thrust calculation

At around 20° angle of attack the lift coefficient of the crescent shaped wing profile for D2R9 and D1R10 seemed to outshine the other sail options. Figure **5-10** presents for the thrust comparison between the different sail types at 20° of angle of attack in which the drag also gets taken into account.

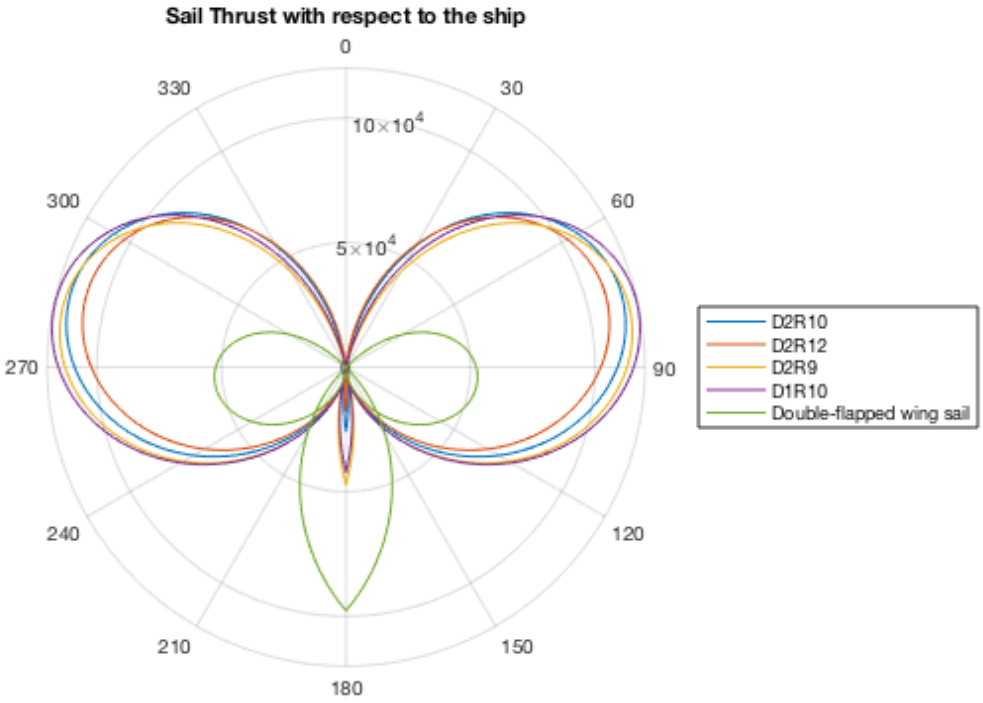

Figure 5-10 *Polar plot of sail thrust for different sail designs*

Figure **5-10** shows for the thin crescent sail to retain the best thrust along a broader span of angles. Even though Figure **5-8** for the case of 20° stated for both D1R10 and D2R9 to sustain similar amount of pressure magnitude, the drag has a significantly larger impact on the sail with increased curvature (D2R9). Through this it can be stated that with correct interface between different parameters on the sail profile, an optimal sail wing can be obtained. All crescent cases indicate for results that overtakes the also studied double-flapped wing sail.

In Figure **5-10** one can also observe for a minor "tail" representing the negative thrust at 180°. Through this point the drag will be predominating factor of the thrust only generating its force as long as the ship speed is lower than the wind speed at low wind angles. The polar plot above represents a case in which the windspeed is given as 8 m/s, ship speed as 12 kn and sail area as 1028 m^2.

6 Conclusion

This report concerns an initial study on how a crescent shaped wing sail behaves by parametrical changes. It can be stated for wind propulsion with the studied sail type to retain thrust forces larger than regular NACA-profiles. To bear in mind is that symmetrical wing profiles have their optimum angle of attack obtained at lower angle of attack rather than the 20° which is the case for the crescent wing profile. With careful consideration of the different parametrical changes one can obtain great thrust force to propel the vessel forward.

With a greater curvature on the sail one can attain very large lift coefficients, but to keep in mind, is the increase of flow separation which will induce a pressure drag and by that reduce the thrust which also can be seen in Figure **5-10**. Thrust is a force affected by both lift and drag, and to achieve the best result is it for most cases necessary to have a large lift coefficient and low drag coefficient. A way to reduce the flow separation occurring at high curvatures is to keep the airfoil as thin as possible. This will reduce the area in which flow separation otherwise would have taken place. In this study, a remarkable difference was noted when the thickness was reduced by 1 meter. The material selection is of high importance since it creates a limitation on how thin the crescent shaped profile can be.

When the symmetrical NACA 0015-profile is studied it can be stated for a remarkably lower amount of flow separation due to its streamlined shape. But as mentioned before, a more streamlined body sustains more frictional drag. One does also notice a reduction in lift for the symmetrical profile, this is due to the smaller curvature that is made as the body keeps its streamlined shape.

When modelling several variations in which comparisons are going to be carried out, it is important to keep a consistent modelling setup to reduce the errors being induced by meshing differently or simply by the selection of turbulence model and boundary layers. Computational fluid dynamics have many different solution prepositions in which researchers still are investigating to attain the most accurate one. Therefore, one can supposedly carry out the initial conditions and results through this type of calculations. Thus, to receive accurate comprehensible results, the CFD studies should always be backed up by experimental testing.

This study has contributed to the understanding of how to compute and study the concept of wing sails. Among current wing profile solutions that are being studied, such as the double-flapped wing sails, the results from this report introduces the crescent shaped wing profile to be considered as a reasonable alternative within profile selection due to its comparably high lift coefficients. It has been shown that entirely focusing on the lift coefficients are not sufficient enough to sustain an understanding over the propulsive effects. As much as lift affects the thrust so does the drag. For seagoing vessels, the lift and drag ratio is not as high of relevance as it is within aviation studies, since these vessels for example utilizes the drag force when sailing downwind. Yet one still has to remember the different aspects that have an impact on the different types of drag forces which are existing. What might be a solution for one type of drag might be a triggering factor for the other, therefore is it out of great interest to study how the forces interact.

The induced drag which is generated through the tip vortices is noted for having an impact on mainly the drag coefficient but also notable impact on the lift coefficient. It is thereby of interest to minimize the occurrence of induced drag. For symmetrical profiles winglets are used minimize the pressure leakage that causes the imbalances on the wing. For the crescent shaped profile this must be further investigated. It can be discussed whether an increase of curvature might actually reduce the need of a winglet as the flow does not have such an easy passage to “spill-over” as the symmetric wing.

For the case of the studied crescent sail profile, it is important to find the balance in which the curvature interacts with the body. A more streamlined body will conclude in more friction drag and more pressure drag will be observed as the chamber or angle of attack increases and flow separation occurs. Lastly to mention is the induced drag which can be simulated in 3D modelling. The occurrence of vortices and circulation is what today plays a huge part in describing lift and drag. Therefore, one has to work with these concepts to better understand the formula of finding the perfect sail. Letting the circular shape of the crescent shaped airfoil interact with the natural flow of the fluid seems to be a succeeding concept in which it creates an opportunity for the fluid traveling in circular pattern to stay attached to its circular motion.

7 Future work

The future of this study beholds a more thorough investigation among different parametric differences. Further one has to take into account for studying the airfoil within a larger angle spectrum. This report beholds de purpose of initiating the understating of the lifting concept and how it systematically can be studied to attain valuable data before actually executing a prototype experimental study.

The concept of aerodynamic includes many details that cannot be neglected, one in which how the aerodynamical forces affects the studied body and surroundings. These types of studies can be carried out through fluid structure interaction (FSI).

8 References

Ahmed, T., Amin, M. T., Islam, S. R., & Ahmed, S. (2013). Computational Study of Flow Around a NACA 0012 Wing Flapped at Different Flap Angles with Varying Mach Numbers. *Global Journal of Researches in Engineering, 13(4), Version 1.0*, 5-16.

AIAA. (2019). 76.6.1 Spalart-Allmaras (SA) Model. *52nd AIAA/SAE/ASEE Joint Propulsion Conference, Salt Lake City, UT, July 25-27, 2016.* American Institute of Aeronautics and Astronautics.

Airfoil Tools. (2021, February). *NACA 0015 (naca0015-il)*. Retrieved from airfoiltools.com: http://airfoiltools.com/airfoil/details?airfoil=naca0015-il

Anderson, R., & Anderson, R. C. (2003). *A Short History of the Sailing Ship.* Mineola: Dover Publications, Inc.

Bisbee, J., Halloran, P., & Larkin, N. (1995). *Sailing & the Tech Dinghy - Instruction maual.* Cambridge, Massachusetts: Massachusetts Institute of Technology.

Blazek, J. (2001). *Computational Fluid Dynamics: Principles and Applications.* Switzerland: Elsevier.

Cleynen, O. (2013). *Boundary layer separation [Figure]*. Retrieved from Wikimedia Commons: https://commons.wikimedia.org/wiki/File:Boundary_layer_separation.svg

Eldredge, J. D. (2019). *Mathematical Modeling of Unsteady Inviscid Flows.* Los Angeles: Springer.

Elkaim, G. H., & Parkinson, W. B. (2001). *System identification for precision control of a wingsailed GPS-guided catamaran.* Stanford: Stanford University.

Eshaan. (2013). *Trade-off relationship between pressure drag and friction drag [Figure]*. Retrieved from Wikimedia Commons: https://commons.wikimedia.org/wiki/File:Pressure_Drag_and_Friction_Drag.png

Ghiaasiaan S, M. (2012). M.1 The Spalart-Allmaras Model. In *Convective Heat and Mass Transfer.* Cambridge University Press.

Hinze, J. O. (1975). *Turbulence (2nd ed.).* New York: McGraw-Hill.

Kuethe, A. M., & Chow, C.-Y. (1998). *Foundations of aerodynamics : bases of aerodynamic design (5th ed.).* New York: Wiley.

Kwang-Yong, K., Abdus, S., Ernesto, & Benini. (2019). *Design Optimization of Fluid Machinery - Applying Computational Fluid Dynamics and Numerical Optimization .* Singapore: John Wiley & Son .

Li, D., Zhang, Y., Li, P., Dai, J., & Li, G. (2019). AERODYNAMIC PERFORMANCE OF A NEW DOUBLE-FLAP WING SAIL. *Polish Maritime Reserch 4, 26(104)*, 61-68.

Li, D., Zhang, Y., Li, P., Dai, J., & Li, G. (2019). AERODYNAMIC PERFORMANCE OF A NEW DOUBLE-FLAP WING SAIL [Figure]. *Polish Maritime Research 4, 26(104)*, 63.

Li, Q., Nihei, Y., Nakashima, T., & Ikeda, Y. (2015). A study on the performance of cascade hard sailsand sail-equipped vessels. *Ocean Engineering (vol. 98)*, 23-31.

Matsumoto, N., Inoue, M., & Sudo, M. (1983). Operating performance of a sail equipped tanker in waves and wind. *Second international conference on*

stability of ships and ocean vehicles '82 (pp. 141-464). Tokyo: Society of naval architects of Japan.
Mises, v. R., & Friedrichs, K. (1971). *Fluid Dynamics - Applied Mathematical Sciences (vol. 5).* New York: Springer-Verlag.
Reitz, R. D., Ogawa, H., Payri, R., Fansler, T., Kokjohn, S., Moriyoshi, Y., . . . Zhao, H. (2020). IJER editorial: The future of the internal combustion engine. *International Journal of Engine Research Vol. 21(1)*, 3–10. https://doi.org/10.1177/1468087419877990.
Rodrigue, J.-P. (2020). *The Geography of Transport Systems 5th ed.* New York: Routledge.
Shukla, P. C., & Ghosh, K. (2009). Revival of the Modern Wing Sails for the Propulsion of Commercial Ships. *World Academy of Science, Engineering and Technology vol (27)*, 398-403.
Siemens. (n.d). *Simcenter Star-CCM+*. (Version 15.06.008) [Siemens PLM Software]: https://www.plm.automation.siemens.com/global/en/products/simcenter/STAR-CCM.html.
Spalart, P. R., & Allmaras, S. R. (1992). A one-equation turbulance model for aerodynamic flows. *AIAA 30th Aerospace Sciences Meeting and Exhibit.* Reno, USA: La Recherche Aérospatiale.
Tam K. W, C. (2015). 15.5.2 RANS Computation: The k - ε Model. In *Computational Aeroacoustics - A Wave Number Approach.* Cambridge University Press.
Wilcox, D. C. (2006). *Turbulance modeling for CFD.* La Cañada, USA: DCW Industries.
Zawawi, M. H., Saleha, A., Salwa, A., Hassan, N. H., Zahari, N. M., Ramli, M. Z., & Muda, Z. C. (2018). A Review: Fundamentals of Computational Fluid Dynamics (CFD). *AIP Conference Proceedings, 2030(1).*
Zimba, J. (2009). *Force and Motion - An Illustrated Guide to Newton's Laws.* Baltimore: Johns Hopkins University Press.
Zucker, R. D., & Biblarz, O. (2020). *Fundamentals of gas dynamic - 3rd ed.* Monterey: John Wiley & Sons.

9 Appendix A

Following table represents the reference data for the NACA-profiles.

Ref: Robert.E, Paul. C (1981)								
	Rn: 5*10^6		Rn: 10*10^6		Rn:5*10^6		Rn: 10*10^6	
	NACA 0012		NACA 0012		NACA 0015		NACA 0015	
Angle [°]	C_D	C_L	C_D	C_L	C_D	C_L	C_D	C_L
1	0,0064	0,0000	0,0064	0,0000	0,0068	0,0000	0,0068	0,0000
2	0,0064	0,1100	0,0064	0,1100	0,0069	0,1100	0,0068	0,1100
3	0,0066	0,2200	0,0066	0,2200	0,0070	0,2200	0,0069	0,2200
4	0,0068	0,3300	0,0068	0,3300	0,0073	0,3300	0,0071	0,3300
5	0,0072	0,4400	0,0071	0,4400	0,0075	0,4400	0,0074	0,4400
6	0,0076	0,5500	0,0074	0,5500	0,0080	0,5500	0,0077	0,5500
7	0,0081	0,6600	0,0078	0,6600	0,0084	0,6600	0,0081	0,6600
8	0,0086	0,7700	0,0082	0,7700	0,0089	0,7700	0,0086	0,7700
9	0,0092	0,8800	0,0086	0,8800	0,0095	0,8800	0,0090	0,8800
10	0,0098	0,9900	0,0091	0,9900	0,0102	0,9900	0,0096	0,9900
11	0,0106	1,1000	0,0097	1,1000	0,0113	1,0685	0,0103	1,1000
12	0,0118	1,1842	0,0104	1,2100	0,0124	1,1553	0,0114	1,1749
13	0,0130	1,2673	0,0116	1,2906	0,0136	1,2290	0,0123	1,2591
14	0,0143	1,3242	0,0127	1,3687	0,0149	1,2847	0,0134	1,3300
15	0,0159	1,3423	0,0141	1,4171	0,0149	1,2847	0,0147	1,3825
16	0,1770	1,3093	0,0157	1,4214	0,0180	1,3298	0,0161	1,4136
17	0,1980	1,2195	0,0185	1,2941	0,0198	1,3186	0,0176	1,4233
18	0,2290	1,0365	0,0210	1,1200	0,0218	1,2917	0,0194	1,4136
19	0,1480	0,9054	0,0241	0,9795	0,0240	1,2576	0,0213	1,3897
20	0,2740	0,8412	0,1610	0,8983	0,0265	1,2242	0,0234	1,3608
21	0,2970	0,8233	0,2970	0,8668	0,1660	1,1965	0,0257	1,3325
23	0,3200	0,8327	0,3200	0,8665	0,3050	1,1771	0,1770	1,3077
24	0,3440	0,8563	0,3440	0,8859	0,3290	1,1647	0,3290	1,2767
25	0,3690	0,8903	0,3690	0,9151	0,3540	1,1611	0,3540	1,1981
26	0,3940	0,9295	0,3940	0,9492	0,3790	1,1563	0,3790	1,1538
27	0,4200	0,9718	0,4200	0,9927	0,4050	1,1322	0,4050	1,1380
28	0,4460	1,0193	0,4450	1,0371	0,4320	1,1268	0,4320	1,1374
29	0,4730	1,0680	0,4730	1,0833	0,4600	1,1397	0,4600	1,1519
30	0,5700	0,9150	0,5700	0,9150	0,5700	0,8550	0,5700	0,8550

10 Appendix B

Following table represents all of the obtained simulation data from Star CCM+.

Table 10-1 *Simulation results from Star CCM+*

Star CCM+ CFD simulations								
Reynolds number: $18.5 \cdot 10^6$								
Crescent wing profile								
Parametric Change	D2R9		D2R10		D2R12		D1R10	
Angle [°]	C_D	C_L	C_D	C_L	C_D	C_L	C_D	C_L
0	0.0673	0.6768	0.0483	0.9727	0.0198	0.9459	0.0502	0.7453
1	0.0704	0.9540	0.0413	1.2235	0.0214	1.0277	0.0519	1.0176
2	0.0753	1.2147	0.0441	1.3844	0.0231	1.1078	0.0536	1.2435
3	0.0794	1.4403	0.0491	1.4836	0.0249	1.1862	0.0543	1.4265
4	0.0820	1.6714	0.0538	1.5669	0.0269	1.2607	0.0598	1.7180
5	0.0893	1.7970	0.0587	1.6459	0.0291	1.3323	0.0639	1.8785
6	0.0971	1.8800	0.0639	1.7200	0.0315	1.4003	0.0700	1.9821
7	0.1056	1.9588	0.0698	1.7920	0.0340	1.4637	0.0753	2.0601
8	0.1134	2.0218	0.0761	1.8613	0.0379	1.5335	0.0804	2.1228
9	0.1219	2.0789	0.0828	1.9254	0.0428	1.6123	0.0885	2.2023
10	0.1309	2.1401	0.0899	1.9835	0.0484	1.6921	0.0966	2.2733
11	0.1405	2.1949	0.0977	2.0403	0.0545	1.7655	0.1047	2.3297
12	0.1505	2.2432	0.1065	2.0934	0.0614	1.8361	0.1132	2.3763
13	0.1625	2.2875	0.1161	2.1443	0.0684	1.8969	0.1232	2.4203
14	0.1747	2.3274	0.1263	2.1902	0.0762	1.9588	0.1334	2.4608
15	0.1881	2.3667	0.1373	2.2308	0.0850	2.0139	0.1446	2.4988
16	0.2015	2.4044	0.1496	2.2674	0.0948	2.0632	0.1571	2.5329
17	0.2168	2.4440	0.1629	2.3032	0.1049	2.1028	0.1709	2.5600
18	0.2330	2.4806	0.1775	2.3306	0.1167	2.1358	0.1859	2.5840
19	0.2502	2.5098	0.1940	2.3563	0.1309	2.1665	0.2014	2.6022
20	0.2682	2.5314	0.2123	2.3792	0.1465	2.1917	0.2203	2.6183
21	0.2881	2.5502	0.2324	2.3938	0.1653	2.2098	0.2409	2.6275
22	0.3099	2.5625	0.2547	2.4070	0.1872	2.2134	0.2633	2.6325
23	0.3338	2.5764	0.2793	2.4169	0.2158	2.2010	0.2892	2.6337
24	0.3607	2.5871	0.3039	2.4133	0.4533	2.2334	0.3169	2.6277
25	0.3873	2.5914	0.3336	2.4066	0.8451	2.3502	0.3471	2.6155
26	0.4185	2.5937	0.3659	2.3997	0.8948	2.1862	0.3834	2.5995
27	0.4536	2.5885	0.4063	2.3865	1.0345	2.2997	0.4271	2.5772
28	0.4857	2.5936	0.4508	2.3612	1.2009	2.3138	0.4780	2.5406
29	0.5290	2.5795	0.8492	2.3088	1.3023	2.2718	0.7890	2.3214
30	0.5723	2.5464	1.1896	2.3834	1.1552	2.0016	1.1451	2.4779

DEPARTMENT OF MECHANICS AND
MARITIME SCIENCE CHALMERS
UNIVERSITY OF TECHNOLOGY
Gothenburg, Sweden 2021
www.chalmers.se

CHALMERS
UNIVERSITY OF TECHNOLOGY